The Astrophysical Journal, 905:87 (17pp), 2020 December 20 https://doi.org/10.3847/1538-4357/abc685

Probing Jet Launching in Neutron Star X-Ray Binaries: The Variable and Polarized Jet of SAX J1808.4–3658

M. C. Baglio[1,2], D. M. Russell[1], S. Crespi[1], S. Covino[2], A. Johar[1], J. Homan[3,4], D. M. Bramich[1], P. Saikia[1], S. Campana[2], P. D'Avanzo[2], R. P. Fender[5], P. Goldoni[6], A. J. Goodwin[7], F. Lewis[8,9], N. Masetti[10,11], A. Miraval Zanon[2,12], S. E. Motta[2,5], T. Muñoz-Darias[13,14], and T. Shahbaz[13,14]
[1] Center for Astro, Particle, and Planetary Physics, New York University Abu Dhabi, P.O. Box 129188, Abu Dhabi, UAE; mcb19@nyu.edu
[2] INAF, Osservatorio Astronomico di Brera, Via E. Bianchi 46, I-23807 Merate (LC), Italy
[3] Eureka Scientific, Inc., 2452 Delmer Street, Oakland, CA 94602, USA
[4] SRON Netherlands Institute for Space Research, Sorbonnelaan 2, 3584 CA, Utrecht, The Netherlands
[5] University of Oxford, Department of Physics, Astrophysics, Denys Wilkinson Building, Keble Road, OX1 3RH, Oxford, UK
[6] APC, Astroparticule et Cosmologie, Université Paris Diderot, CNRS/IN2P3, CEA/Irfu, Observatoire de Paris, Sorbonne Paris Cité, 10, Rue Alice Domon et Léonie Duquet, F-75006 Paris, France
[7] School of Physics and Astronomy, Monash University, Clayton, 3800, Australia
[8] Faulkes Telescope Project, School of Physics and Astronomy, Cardiff University, The Parade, Cardiff, CF24 3AA, Wales, UK
[9] Astrophysics Research Institute, Liverpool John Moores University, 146 Brownlow Hill, Liverpool L3 5RF, UK
[10] INAF–Osservatorio di Astrofisica e Scienza dello Spazio, via Piero Gobetti 93/3, I-40129 Bologna, Italy
[11] Departamento de Ciencias Fisicas, Universidad Andrés Bello, Av. Fernández Concha 700, 7591538 Las Condes, Santiago, Chile
[12] Università dell'Insubria, Dipartimento di Scienza e Alta Tecnologia, Via Valleggio 11, I-22100, Como, Italy
[13] Instituto de Astrofísica de Canarias, E-38205 La Laguna, Tenerife, Spain
[14] Departamento de Astrofísica, Universidad de La Laguna, E-38206 La Laguna, Tenerife, Spain
Received 2020 July 10; revised 2020 October 25; accepted 2020 October 28; published 2020 December 16

Abstract

We report on an optical photometric and polarimetric campaign on the accreting millisecond X-ray pulsar (AMXP) SAX J1808.4–3658 during its 2019 outburst. The emergence of a low-frequency excess in the spectral energy distribution in the form of a red excess above the disk spectrum (seen most prominently in the *z*, *i*, and *R* bands) is observed as the outburst evolves. This is indicative of optically thin synchrotron emission due to a jet, as seen previously in this source and in other AMXPs during outburst. At the end of the outburst decay, the source enters a reflaring state. The low-frequency excess is still observed during the reflares. Our optical (*BVRI*) polarimetric campaign shows variable linear polarization (LP) throughout the outburst. We show that this is intrinsic to the source, with low-level but significant detections (0.2%–2%) in all bands. The LP spectrum is red during both the main outburst and the reflaring state, favoring a jet origin for this variable polarization over other interpretations, such as Thomson scattering with free electrons from the disk or the propelled matter. During the reflaring state, a few episodes with stronger LP levels (1%–2%) are observed. The low-level, variable LP is suggestive of strongly tangled magnetic fields near the base of the jet. These results clearly demonstrate how polarimetry is a powerful tool for probing the magnetic field structure in X-ray binary jets, as for active galactic nuclei jets.

Unified Astronomy Thesaurus concepts: Jets (870); Low-mass x-ray binary stars (939); Neutron stars (1108); Compact objects (288); Stellar accretion disks (1579)

Supporting material: data behind figure

1. Introduction

Millisecond pulsars (MSPs) are low–magnetic field ($\sim 10^8$ G) neutron stars (NSs) emitting pulsed radiation with a periodicity of 1–10 ms (typically in the radio band but also in X- and γ-rays). The most accredited scenario able to explain the existence of such objects is the so-called recycling scenario of MSPs (e.g., Srinivasan 2010). According to this, MSPs are NSs that have been accelerated or recycled (i.e., switched on again with a lower magnetic field and longer rotational period) through accretion, typically in low-mass X-ray binaries (LMXBs; Alpar et al. 1982; Radhakrishnan & Srinivasan 1982). After decades of search, the first LMXB pulsating in X-rays at the millisecond period (an accreting millisecond X-ray pulsar (AMXP)) was discovered in 1998 (SAX J1808.4–3658; Wijnands & van der Klis 1998), with 2.49 ms X-ray pulsations, showing that NSs in LMXBs can indeed spin very rapidly. This conclusion was then reinforced with the detection of coherent X-ray pulsations in the millisecond regime in other LMXBs. Twenty-two AMXPs have been discovered so far (for reviews see Patruno & Watts 2012; Campana & Di Salvo 2018).

Optical and near-infrared (NIR) light emitted from AMXPs (and NS-LMXBs in general) is traditionally thought to originate in the reprocessing of the X-ray thermal emission from the accretion disk; this process is dominant during outbursts in transient systems, whereas during quiescence the major contribution at these wavelengths is given by the low-mass companion star. In addition, evidence for the emission of relativistic jets has been found at optical–NIR (OIR) frequencies. Russell et al. (2007) showed that reprocessing of X-ray thermal emission from accretion disks cannot explain the observed OIR fluxes in Atoll sources and AMXPs in their high-luminosity states (as well as those for black hole LMXBs (BH-LMXBs) in hard X-ray states). In particular, optically thin synchrotron emission from jets is found to dominate NIR light when $L_X > 10^{36}$ erg s^{-1} and optical light when $L_X > 10^{37}$ erg s^{-1} (Russell et al. 2007). For NS-LMXB Z-sources, X-ray reprocessing can instead explain well the observed OIR

fluxes, with synchrotron emission possibly contributing to the NIR in most cases (Russell et al. 2007).

Evidence for the production of relativistic jets in AMXPs can be found from radio detections (e.g., Gaensler et al. 1999; Tudor et al. 2017 and references therein) and OIR spectral energy distributions. If a jet is produced, a flux excess at the lowest OIR frequencies can be observed, due to the superposition of the optically thin synchrotron jet spectrum and the low-frequency tail of the blackbody of the reprocessed accretion disk. This excess has been observed in four AMXPs so far (Russell et al. 2007): XTE J1814–338 (Krauss et al. 2005) during outburst (evidence of a quiescent residual jet is also reported in Baglio et al. 2013), SAX J1808.4–3658 (Wang et al. 2001; Greenhill et al. 2006; Baglio et al. 2015), IGR J00291+5934 (Torres et al. 2008; Lewis et al. 2010), and XTE J0929–314 (Giles et al. 2005). NIR excess has also been detected in other NS-LMXBs (e.g., Callanan et al. 2002; Migliari et al. 2010; Harrison et al. 2011, 2014; Baglio et al. 2014b, 2016b, 2019c; Wang & Wang 2014; see Saikia et al. 2019 and references therein for examples of NIR excesses in black hole LMXBs). At lower frequencies, the spectrum of the jet is optically thick, characterized by a flat or slightly inverted radio slope. The break between the optically thick and thin spectra typically falls in the NIR (jet break frequency; Falcke et al. 2004). The break has been detected in the NS-LMXBs 4U 0614+091 and Aql X–1 (Migliari et al. 2010; Díaz Trigo et al. 2018) and in the BH-LMXBs GX 339-4 (Corbel & Fender 2002; Cadolle Bel et al. 2011; Gandhi et al. 2011; Corbel et al. 2013), XTE J1118+480 (Hynes et al. 2006), V404 Cyg (Russell et al. 2013a; Tetarenko et al. 2019), XTE J1550-564 (Chaty et al. 2011), MAXI J1836–194 (Russell et al. 2013b), and MAXI J1535–571 (Russell et al. 2020).

Synchrotron emission is one of the physical processes capable of generating linearly polarized radiation, up to very high levels (Rybicki & Lightman 1979). Thus the case is strong that there can be a significant presence of linearly polarized emission from LMXBs that hints at the presence of jets. In particular, different behaviors of the linear polarization (LP) are expected, depending on the frequency of the observation. If the frequency is in the optically thick jet spectrum regime, a maximum of a few percent LP is generally observed (e.g., Fender 2001). An optically thin synchrotron could, in contrast, produce LP up to ∼70% (Blandford et al. 2002); however, in NIR observations (i.e., close to the jet break frequency), this typically translates into a significantly lower value due to the low ordering of magnetic field lines in the jet (as in the case of the NS-LMXB 4U 0614+091; Baglio et al. 2014b). Nevertheless, some LMXBs showing up to 30% LP have been found, indicating that a high level of magnetic field line ordering for LMXBs is also possible (Fender 2001; see the case of the BH-LMXB Cyg X-1 reported in Russell & Shahbaz 2014). Polarimetry therefore has the power to probe the magnetic field structure in jets.

At optical frequencies, however, the expected LP should never exceed a few percent, due to the dominant emission coming from nonpolarized sources at those frequencies, such as the accretion disk or the companion star (Shahbaz et al. 2008). See Shahbaz (2019) for a recent review on polarimetry of LMXBs. OIR LP can also arise from different processes, like the electronic (Thomson) scattering of radiation with free electrons that can be found, e.g., in a geometrically symmetrical accretion disk that is mostly ionized. Since each electron that is responsible for scattering in the disk oscillates in principle in a random direction, a very low and constant level of LP is expected (a few percent at the maximum), and the LP will be higher for higher frequencies, following the spectrum of the accretion disk. Sometimes, a significant phase-dependent variability of the polarization with the orbital period can be observed (see, e.g., the cases of GRO J1655–40, Her X–1, and PSR J1023+0038; Gliozzi et al. 1998; Schultz et al. 2004; Baglio et al. 2016a).

2. SAX J1808.4–3658

The X-ray binary SAX J1808.4–3658 (hereafter SAX J1808) is an X-ray transient discovered in 1996 (in't Zand et al. 1998) at a distance of 2.5–3.5 kpc (in't Zand et al. 1998; Galloway & Cumming 2006). It is the first AMXP to be discovered (Wijnands & van der Klis 1998), the compact object being a 401 Hz (∼2.5 ms) X-ray pulsar. The companion star has been proposed to be a semi-degenerate star with a mass of ∼0.05–0.10 $M_{\odot}$ (Bildsten & Chakrabarty 2001; Wang et al. 2001; Deloye et al. 2008). The system has an orbital period of ∼2 hr (Chakrabarty & Morgan 1998), and the NS magnetic field has been inferred to be $\sim 10^8$ G (Psaltis & Chakrabarty 1999).

SAX J1808 displays recurrent outbursts. To date, nine outbursts have been observed (in 1996, 1998, 2000, 2002, 2005, 2008, 2011, 2015, and 2019), with a recurrence time of 2–4 yr. These events typically show a main outburst with a fast rise and a subsequent slow decay. After this phase, which lasts for approximately 1 month, a reflaring period at low X-ray luminosities (10^{32-35} erg s^{-1}) is seen, which persists for tens of days (see, e.g., Wijnands et al. 2001; Patruno et al. 2016). This reflaring state has been explained by invoking a propeller scenario, with a large amount of matter expelled from the system, or the presence of a trapped disk truncated at the co-rotation radius (Patruno et al. 2016).

Optical and infrared photometry of the system during its 1998 outburst revealed the presence of a clear infrared excess with respect to the expected low-frequency blackbody tail of the accretion disk and/or companion star (Wang et al. 2001), which was again seen in the 2005 outburst (Greenhill et al. 2006). This behavior is similar to what has been observed in the case of other AMXPs (e.g., XTE J1814–338, IGR J00291 +5934, XTE J0929–314; e.g., Giles et al. 2005; Krauss et al. 2005; Lewis et al. 2010) and has been indirectly linked to synchrotron emission from jets during outburst (signatures of a quiescent, receding jet have also been reported for XTE J1814–338 in Baglio et al. 2013).

During the 2015 outburst, an infrared (*H*-band) excess was observed, as reported in Baglio et al. (2015). Additionally, NIR polarimetry was obtained with the SofI instrument mounted on the New Technology Telescope (NTT, La Silla, Chile; ID: 295. D-5012; principal investigator (PI): Baglio), with the aim of confirming the synchrotron nature of the NIR emission. See Section 5 for further details on this.

SAX J1808 has been monitored at optical wavelengths since 2008 with the Las Cumbres Observatory (LCO) network of robotic 1 m and 2 m telescopes, including the 2 m Faulkes Telescope South at Siding Spring, Australia (Elebert et al. 2009; Tudor et al. 2017). As part of this campaign, after several years of quiescence, between 2019 July 25 and 30 a brightening was observed (Russell et al. 2019b) and interpreted as the beginning stages of a new outburst or as an optical

Table 1
Detailed Log of the VLT/FORS2 Polarimetric Observations Performed between 2019 August 8 and 2019 September 24

Epoch (UT) (Label)	MJD (Start)	Filter	Exp. Time (s)	Sky Transp.
2019-08-08	58703.2102332	*b*	80	CLR
(Epoch 1)		*v*	40	CLR
2019-08-13	58708.2469446	*b*	80	THN
(Epoch 2)		*v*	40	THN
		R	40	THN
		I	60×2	THN
2019-08-16	58711.1873337	*b*	80	CLR
(Epoch 3)		*v*	40	CLR
		R	40	CLR
		I	60×2	CLR
2019-08-18	58713.1245152	*b*	80	THICK
(Epoch 4)		*v*	60	THICK
		R	60	THICK
		I	80×2	THICK
2019-08-21	58716.1522254	*b*	80	CLR
(Epoch 5)		*v*	60	CLR
		R	60	CLR
		I	80×2	CLR
2019-08-24	58719.9839237	*b*	80	CLR
(Epoch 6)		*v*	80	CLR
		R	80	CLR
		I	100×2	CLR
2019-09-04	58730.9961515	*b*	120	THN
(Epoch 7)		*v*	100	THN
		R	70	THN
		I	130×2	THN
2019-09-07	58733.0045035	*b*	150	CLR
(Epoch 8)		*v*	100	CLR
		R	110	CLR
		I	180×2	CLR
2019-09-25	58751.0161424	*b*	150	CLR
(Epoch 9)		*v*	100	CLR

Note. In the last column, the sky transparency is reported. On the European Southern Observatory (ESO) website, clear conditions (CLR) imply less than 10% of the sky (above 30 degrees elevation) is covered in clouds and transparency variations are under 10%; thin conditions (THN) imply transparency variations above 10%; and thick conditions mean that large transparency variations are possible, which is equivalent to not having constraints on the transparency conditions (https://www.eso.org/sci/observing/phase2/ObsConditions.VISIR.html).

precursor (see, e.g., Bernardini et al. 2016; Russell et al. 2019a). The brightening was not observed in the X-rays until August 6 with Swift/XRT (Goodwin et al. 2019) and NICER (Goodwin et al. 2020). According to NICER observations, the outburst reached its peak on August 13, after which it started to decay (Bult et al. 2019a). On August 24 the source entered its reflaring state, starting to alternate between lower ($\sim 10^{32}$ erg s^{-1}) and higher ($\sim 10^{33}$ erg s^{-1}) luminosity periods on timescales of about a day (Bult et al. 2019a). The reflaring state was also observed at optical frequencies thanks to the ongoing Faulkes/LCO monitoring (Baglio et al. 2019a). At the beginning of 2019 October, optical observations revealed that the source was back to its quiescent level (Baglio et al. 2019b).

3. Observations and Data Analysis

SAX J1808 was extensively monitored during its 2019 outburst using the LCO 2 m (Faulkes) and 1 m telescopes in the *B*, *V*, *R*, and *i*′ optical bands and with the Very Large Telescope (VLT) in Cerro Paranal, Chile, equipped with the FORS2 instrument used in polarimetric mode (*B*, *V*, *R*, and *I* bands; program ID: 0103.D-0575; PI: Baglio).

3.1. VLT Polarimetry

We observed SAX J1808 with VLT/FORS2 in polarimetric mode with the optical filters *I*_BESS+77, *R*_SPECIAL+76, *v*_HIGH+114, and *b*_HIGH+113 (*I*, *R*, *V*, and *B*) for nine epochs between 2019 August 8 and 2019 September 24, covering approximately the entire outburst. Most observations were performed under optimal sky transparency conditions, which are required in order to obtain a good signal-to-noise ratio in the polarimetric images.

A Wollaston prism was inserted in the optical path, which allowed incident radiation to be split into two simultaneous beams characterized by orthogonal polarization. The two beams are commonly referred to as ordinary (o) and extraordinary (e). To avoid overlapping of the beams on the charge-coupled device, a Wollaston mask was also introduced. Finally, the instrument made use of a rotating half-wave plate (HWP) to take images at four different angles Φ_i with respect to the telescope axis: $\Phi_i = 22.^{\circ}5\,(i-1)$, $i = 1, 2, 3, 4$. A log of the observations is reported in Table 1. All images were reduced by subtracting an average bias frame and dividing by a normalized flat field. Aperture photometry was then performed using the `daophot` tool (Stetson 2000). The normalized Stokes parameters for the LP, Q and U, were defined as follows:

$$Q = \frac{F(\Phi_1) - F(\Phi_3)}{2}, \quad U = \frac{F(\Phi_2) - F(\Phi_4)}{2}, \tag{1}$$

where

$$F(\Phi_i) = \frac{f^{\rm o}(\Phi_i) - f^{\rm e}(\Phi_i)}{f^{\rm o}(\Phi_i) + f^{\rm e}(\Phi_i)}, \tag{2}$$

with $f^{\rm o}$ and $f^{\rm e}$ being the ordinary and extraordinary beam fluxes, respectively. These parameters then needed to be corrected for the instrumental polarization, which could be estimated thanks to the observation of a nonpolarized standard star.[15] For FORS2, unpolarized standard stars are frequently observed in order to monitor the level of the instrumental polarization,[16] which has been stable during the last 10 yr in all bands, at a very low level (0%–0.3%).

Using these corrected Stokes parameters, one could evaluate the level of LP (P) and the angle of polarization (PA) θ as $P = (Q^2 + U^2)^{0.5}$ and $\theta = (1/2)\tan^{-1}(U/Q)$. The PA then needed to be corrected for instrumental effects, which could be estimated thanks to the observation of a highly polarized standard star whose PA was known and tabulated.

However, P is not distributed as a Gaussian (Wardle & Kronberg 1974). In order to take this into account, as shown in Wardle & Kronberg (1974), it would be necessary to add a bias

[15] https://www.eso.org/sci/facilities/paranal/instruments/fors/tools/FORS1_Std.html
[16] http://www.eso.org/observing/dfo/quality/FORS2/reports/FULL/trend_report_PMOS_inst_pol_FULL.html

correction to the measured polarization, which can become very large in the case of low polarization and large errors, typically the case for LMXBs.

3.1.1. The S Parameter Method

A very accurate algorithm has been developed in order to estimate the LP of a source, accounting for all the factors mentioned above, such as the non-Gaussian distribution of P and the possible interstellar contribution to the measured LP (e.g., di Serego Alighieri 1997 and references therein; see also Covino et al. 1999; Baglio et al. 2014a). This algorithm consists of the evaluation of the parameter $S(\Phi)$ for each HWP angle Φ, defined as follows:

$$S(\Phi) = \left(\frac{f^{o}(\Phi)/f^{e}(\Phi)}{f_{u}^{o}(\Phi)/f_{u}^{e}(\Phi)} - 1\right) \Bigg/ \left(\frac{f^{o}(\Phi)/f^{e}(\Phi)}{f_{u}^{o}(\Phi)/f_{u}^{e}(\Phi)} + 1\right), \quad (3)$$

which combines the ordinary and extraordinary fluxes for each HWP angle Φ measured for the target ($f^{o}(\Phi)$ and $f^{e}(\Phi)$, respectively) with the same quantities measured for an unpolarized (u) field star ($f_{u}^{o}(\Phi)$, $f_{u}^{e}(\Phi)$). This parameter can be considered as the component of the normalized Stokes vector that describes the LP along the direction Φ (for example, $S(\Phi = 0) = Q$). This quantity is then related to the polarization P of the target and to the PA θ by the following relation:

$$S(\Phi) = P \cos 2(\theta - \Phi). \quad (4)$$

Therefore, from the fit of the S parameter with Equation (4), one can obtain an accurate estimate of the LP and PA for the target (the latter however will still need to be corrected using the measured angle of a polarized standard star). Moreover, this method can become even more accurate by considering more than one reference field star. In this way, if n is the number of reference field stars, we will end up with n different S values for each angle, which will allow us to derive the probability distribution of $S(\Phi)$ without approximating it with a Gaussian function. The only assumption for this algorithm is that the chosen field stars are considered to be intrinsically unpolarized or to be polarized only by the interaction with the interstellar medium (which we can suppose to be almost the same for the field stars and for the target itself). We noticed that the majority of the reference stars chosen for this work have a Gaia DR2 position, and they were found to be all quite close to Earth, with an average distance of 2.5 ± 0.6 kpc (i.e., very similar to the one inferred for SAX J1808; in't Zand et al. 1998). According to Serkowski et al. (1975), it is possible to evaluate the maximum interstellar contribution to the LP ($P_{\rm int}$) that we expect to observe for any target, depending on its absorption coefficient in the V band (A_V). In particular, $P_{\rm int} < 3A_V$. For SAX J1808, the hydrogen column density $N_{\rm H}$ was measured during the last outburst to be $(1.46 \pm 0.12) \times 10^{21}$ cm^{-2} (Di Salvo et al. 2019); considering the relation between $N_{\rm H}$ and A_V for our Galaxy reported in Foight et al. (2016), we obtained a dust extinction of $A_V = 0.51 \pm 0.04$ and therefore $P_{\rm int} < 1.53\%$. In addition, as already mentioned, the instrumental polarization for the FORS2 instrument was expected to be very low (see footnote 16; in our campaign we also observed a nonpolarized standard star in three different epochs, always obtaining 3σ upper limits to P of $\sim 0.5\%$ in all bands).

To verify that the chosen field stars are intrinsically unpolarized, we plotted them in the P–θ plane. Ideally, the reference stars should all cluster around a common point in the plane with small dispersion, for each epoch and band of observation; any deviation of the centroid of their distribution from the origin of the plane is therefore a good estimate of the average instrumental and/or interstellar polarization along the line of sight. In Figure 1 we show this graph for one band and one epoch (I band on August 15) for the target and for the group of reference stars. To build this figure, LP and PA values were evaluated for each object starting from their Stokes parameters Q and U (Equation (1)). No correction was applied to the LP and PA values of any object at this stage. It is evident from the figure that the reference stars all cluster around a common value in the plane. The instrumental and interstellar LP estimated from this graph is low as expected (<1%, consistent with what is obtained from Serkowski et al. 1975). The PA of the group of reference stars is always of the order of ~150°, in all epochs and bands.

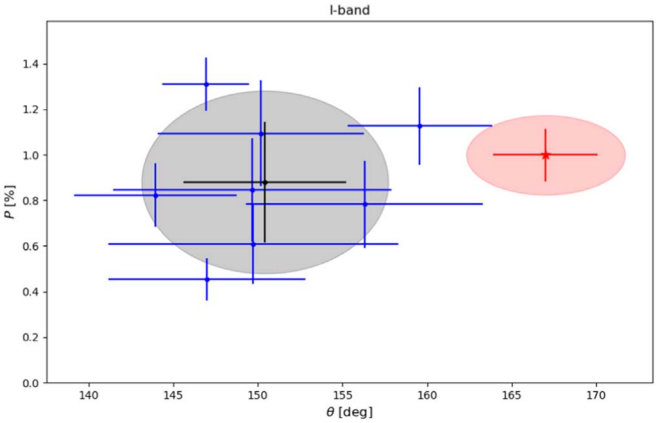

Figure 1. Representation of P vs. θ for the I-band observation of 2019 August 15. With blue dots, the reference stars are plotted (the black dot is the average of the reference stars). SAX J1808 is shown in red. The error of the average was evaluated as the standard deviation of the N reference stars, divided by the square root of N, to account for the dispersion of the reference stars. Gray and red ellipsoids show the 68% confidence level regions for the average of the reference stars and for the target, respectively.

In addition, we did not expect the polarization of the field stars to change from night to night. Therefore, the results of the analysis can become even more accurate by taking into account every epoch of all the reference stars on all nights to correct the target values. The correction will be different from band to band. This is a good procedure because it allows any possible variability due to, for example, a different choice of reference stars from night to night to average out and provides more homogeneous results.

Once $S(\Phi)$ was calculated, P and θ were determined by maximizing the Gaussian likelihood function by an optimization algorithm (e.g., the Nelder–Mead algorithm; Gao & Han 2012) and integrating the posterior probability density of the parameters of our models by a Markov Chain Monte Carlo algorithm (Hogg & Foreman-Mackey 2018) based on the "affine-invariant Hamiltonian" algorithm (Foreman-Mackey et al. 2013). We started the chains from small Gaussian balls centered on the best-fit values. The first third of each chain (the "burn-in phase") was discarded, and we checked that a stationary distribution was reached (Sharma 2017). Fit quality was evaluated as in Lucy (2016). The reported values for P and θ and their 1σ uncertainties are the 0.16, 0.50, and 0.84 quantiles of the posterior distribution of the parameters. Therefore, in general, each P–θ pair taken together is not

necessarily the best-fit solution, although in most cases these values are very close to the maximum a posteriori estimates (see Hogg & Foreman-Mackey 2018 for an extensive discussion).

Finally, the value of θ obtained with this method was corrected by an additional factor from the observation of a polarized standard star with a known and tabulated PA. The resulting average correction was very small in all bands and epochs ($<2°$).

3.2. LCO Monitoring

We observed SAX J1808 with the LCO 2 m Faulkes and 1 m network for the whole duration of the outburst, as part of a monitoring campaign of ∼50 LMXBs (coordinated by the Faulkes Telescope Project[17]; Lewis et al. 2008). Imaging data were taken in the *B*, *R*, and *V* Bessell filters and the Sloan Digital Sky Survey (SDSS) u', i', and z' filters (436.1–870 nm). Since the field is extremely crowded, the source was blended with a few nearby stars especially when SAX J1808 was faint (near and in quiescence), depending on the seeing conditions. In the majority of images, however, the target could be disentangled and multi-aperture photometry (MAP; see Stetson 1990) was performed by the newly developed X-Ray Binary New Early Warning System (XB-NEWS) pipeline (Russell et al. 2019a). The pipeline automatically downloads new images of all targets that are monitored with LCO and all their associated calibration data; then, it performs several quality control steps, computes an astrometric solution for each image using Gaia DR2 positions,[18] performs MAP (along with standard aperture photometry), solves zero-point calibrations between epochs as described in Bramich & Freudling (2012), and flux-calibrates the photometry using the ATLAS-REFCAT2 catalog (which includes the Pan-STARRS[19] DR1, APASS,[20] and other catalogs; Tonry et al. 2012). The *R* band is calibrated indirectly via comparison with predicted *R*-band standard magnitudes. The predicted *R*-band standard magnitudes are computed for ATLAS-REFCAT2 stars with Pan-STARRS1 $g_{\rm P1}$ and $r_{\rm P1}$ standard magnitudes using the transformations provided in Tonry et al. (2012). The pipeline then produces a calibrated light curve for the target with near real-time measurements (for more details see Russell et al. 2019a; Pirbhoy et al. 2020). In cases for which the target was not automatically detected above the detection threshold by the pipeline, XB-NEWS performed forced MAP at the known position of the source. All magnitudes derived from forced photometry with an uncertainty of >0.25 mag were considered unreliable and were therefore rejected.

Observations on the same dates of the VLT polarimetric data were taken in several filters. A detailed observation log of the LCO data can be found in Table 2.

4. Results

In Figure 2 the main results of this campaign are shown. The i'-band light curve obtained with LCO (upper panel) shows the main outburst, which is also clearly observed in the NICER X-ray light curve (second panel; see Bult et al. 2020; Goodwin et al. 2020 for details of the NICER campaign), followed by a reflaring state, with optical reflares of amplitudes of ∼0.5 mag. We note that prior to MJD 58701 (August 6) all the NICER observations were background dominated; therefore, we took an upper limit of 1.37 counts s^{-1}, i.e., the average pre-outburst net count rate plus three times the 1σ standard deviation, as the detection limit for SAX J1808 (Goodwin et al. 2020). By comparing the optical to the X-ray light curve, we can see that the peak of the outburst was first reached in the optical at MJD ∼58706 (August 11) and then in the X-rays at MJD 58709 (August 14; see also Goodwin et al. 2020). A small optical brightening at almost the same time as the onset of the X-ray reflaring state is observed, possibly suggesting similar starting times of the reflaring state in the two bands (this will be discussed in more detail in a follow-up paper; see D. M. Russell et al. 2020, in preparation). In the third panel of Figure 2 we report the evolution of the $V - i'$ absorbed color during the outburst (evaluated using the LCO data). The $V - i'$ color first decreases during the initial rise, then starts to increase during the fast rise of the outburst, meaning that the system is becoming first bluer, then redder. $V - i'$ reaches its peak value at the same time as the main outburst peaks and then decreases with the luminosity, indicating that the spectrum of the source is becoming bluer during the fade from the main peak. Therefore, the behavior of the $V - i'$ color suggests the existence of a red component that brightens during the outburst rise and then fades as the outburst decays. During the reflaring state, more scatter is observed in $V - i'$, hinting that there is a variable component or suggesting the presence of short-timescale variability, which was not possible to properly sample for all epochs with the LCO monitoring campaign (see Figure 3).

To investigate a possible optical short-timescale variability, we looked at two i'-band fast-timing (2 minute binning) light curves obtained using LCO data acquired on MJD 58709 (August 14; at the peak of the outburst) and on MJD 58722 (August 27; at the very beginning of the reflaring state; see Table 2). Both curves show signs of fast variability, with a measured fractional rms of $(3 \pm 1)\%$ on MJD 58709 over a 40 minute timescale (see Figure 3). The fractional rms is, in contrast, not significant on MJD 58722. This hints at the presence of a rapidly (on timescales of tens of minutes) variable component in the optical emission throughout the outburst.

The last two panels of Figure 2 show the results of the VLT polarimetric campaign (see also Table 1). Analysis of the data (performed as described in Section 3.1) allowed us to reach very high precision in the determination of the fractional LP in the case of a detection, with errors of ∼5%–20% of the polarization level, depending on the night (see Table 1). The results are reported in Table 3.

We obtained several significant detections of LP in all bands. In cases of nonsignificant detections, we evaluated 3σ upper limits in all bands, which are also reported in Table 3 and are all quite constraining ($<1\%$), except for the few epochs in which the signal-to-noise ratio was too low, due to bad seeing or thick sky transparency.

For the epochs in which a detection of polarization was observed, we also evaluated the PA. In Figure 4 we show the polarization level *P* versus the PA in all bands. The PA appears to be clustered around ∼0°–50°, and no clear correlation between the two quantities can be found in any of the bands.

[17] http://www.faulkes-telescope.com/
[18] https://www.cosmos.esa.int/web/gaia/dr2
[19] https://panstarrs.stsci.edu
[20] https://www.aavso.org/apass

Table 2
Log of the LCO Observations Published in This Work

Epoch (UT)	MJD	Site	Filters	Exposure (s)	Epoch (UT)	MJD	Site	Filters	Exposure (s)
2019-08-08	58703.195069	1m-C	B	200		58719.876733	1m-C	B	60
(Epoch 1)	58703.183335	1m-C	V	100		58719.869932	1m-C	V	60
	58703.192862	1m-C	R	100	(Epoch 6)	58719.875553	1m-C	R	60
	58703.181707	1m-C	i'	100	2019-08-24	58719.868769	1m-C	i'	60
	58703.186128	1m-C	z'	300		58719.871904	1m-C	z'	200
2019-08-13	58708.789980	1m-S	B	30	2019-09-07	58732.748023	1m-S	i'	200
(Epoch 2)	58708.785300	1m-S	V	30					
	58708.789043	1m-S	R	30					
	58708.784367	1m-S	i'	30					
	58708.786590	1m-S	z'	100					
2019-08-14	58709.799704	1m-S	i'	20 × 100	2019-09-04	58731.545601	1m-C	B	100
					(Epoch 7)	58731.537881	1m-C	V	100
						58731.535669	1m-C	i'	200
						58731.540106	1m-C	z'	200
2019-08-16	58710.836103	1m-S	B	40	2019-09-07	58732.748023	1m-S	i'	200
(Epoch 3)	58710.831429	1m-S	V	40	(Epoch 8)				
	58710.835160	1m-S	R	40					
	58710.830488	1m-S	i'	40					
	58710.832717	1m-S	z'	100					
2019-08-17	58712.855179	1m-A	B	40	2019-09-25	58751.849739	1m-S	B	200
(Epoch 4)	58712.850531	1m-A	V	40	(Epoch 9)	58751.840343	1m-S	V	100
	58712.854255	1m-A	R	40		58751.847530	1m-S	R	100
	58712.849606	1m-A	i'	40		58751.838130	1m-S	i'	200
	58712.851805	1m-A	z'	100		58751.842553	1m-S	z'	200
2019-08-21	58716.859265	1m-S	B	60					
(Epoch 5)	58716.852543	1m-S	V	60					
	58716.858100	1m-S	R	60					
	58716.851378	1m-S	i'	60					
	58716.854512	1m-S	z'	200					

Note. The epochs included are those close in time to the VLT observations (Epochs 1–9) and two data sets in which timing observations were taken (MJD 58709 and 58722). 1m-A, 1m-C, and 1m-S are the 1 m nodes in Australia, Chile, and South Africa, respectively.

4.1. The Moon Contribution

Our polarimetric monitoring covered more than 30 days (Table 1). Therefore, the phase of the Moon considerably changed, as did its separation from the target. The presence of the Moon could alter the measured LP due to reflection, mostly in the B and V bands. We therefore looked for a correlation between (i) the fraction of lunar illumination (FLI) and the measured level of polarization of the target P (%) and between (ii) the Moon–target separation on the sky (deg) and P. In particular, the FLI was defined as the fraction of the lunar disk that is illuminated at local midnight, and it was equal to 1 when the disk was "fully illuminated" and to 0 when the Moon was below the local horizon. The results of the analysis are shown in Figure 5 for the B band and I band.

A hint of a correlation is present in both figure panels in the B band, with a level of LP that increases with increasing FLI (the Pearson correlation coefficient R for this correlation is 0.59) and decreasing Moon–target separation ($R \sim -0.64$). In particular, most upper limits are found at low FLI, i.e., when the effect of reflection should be at its minimum. In the I band, in contrast, no correlation seems to be present ($R \sim 0.02$ for the Moon–target separation and $R \sim -0.40$ for the FLI). Results similar to the I-band ones were also obtained in the R and V bands, with no correlation of the LP of SAX J1808 to the FLI of the Moon or to the Moon–target angular separation in the sky.

We therefore conclude that the B-band polarization detections reported in this work were affected by the presence of the Moon, and the detected variability of the polarization level in this band is therefore likely to be not entirely intrinsic to the target. We will therefore exclude the B-band results from the interpretation of our results. We notice that, as is visible in Figure 2, the measured B-band polarization levels do not stand out from other bands' results, despite the additional contribution of the Moon. This is however in agreement with our conclusions, since the polarization level induced in the optical by the presence of the Moon should not exceed a few percent, which is a level comparable to that due to the emission of synchrotron radiation or to Thomson scattering with free electrons.

4.2. Interstellar Polarization

Using the average Q and U Stokes parameters of all reference stars on all nights of our monitoring, we could derive the polarization introduced due to interstellar and instrumental effects. Since instrumental polarization is negligible, this value

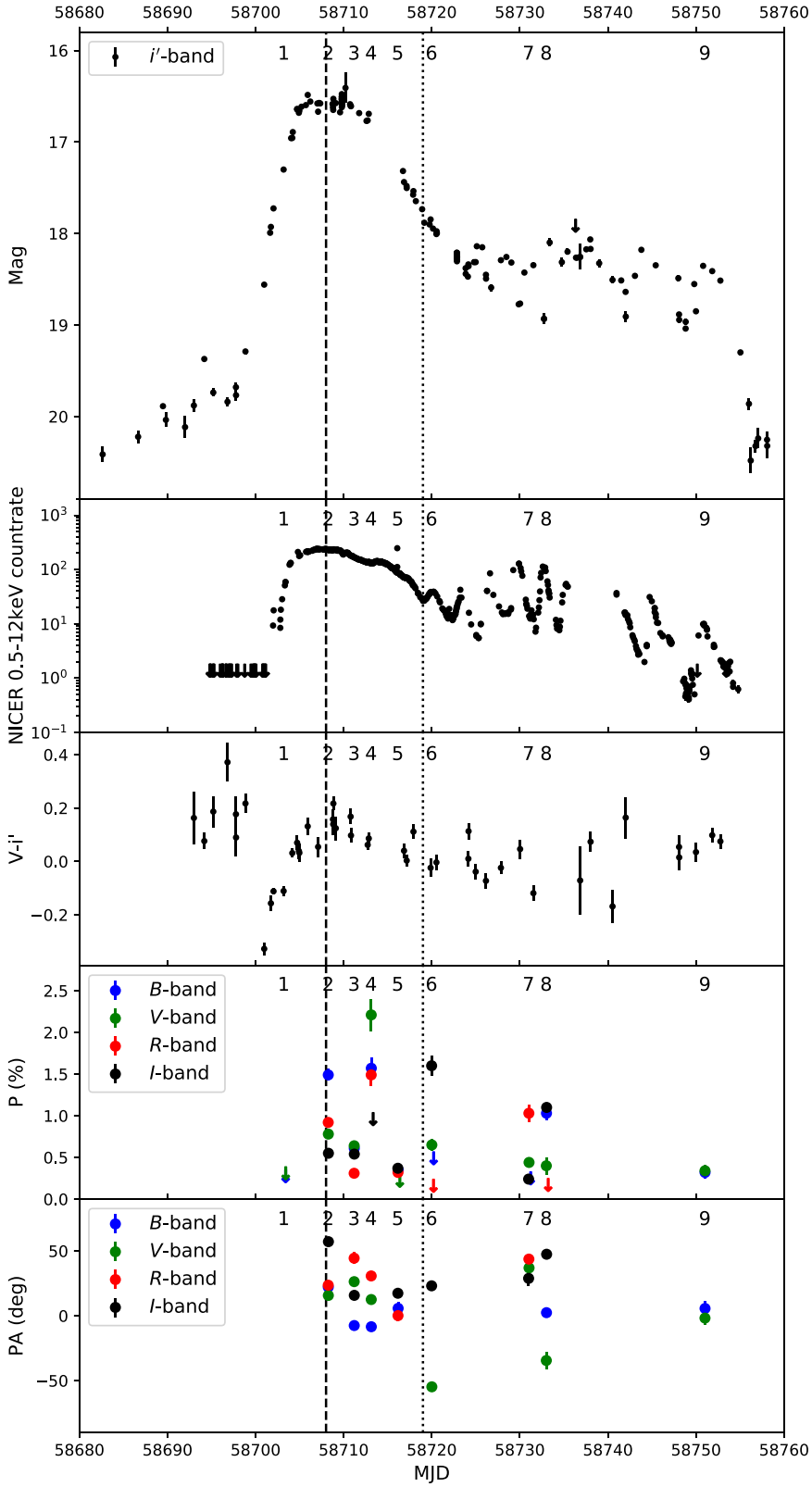

Figure 2. From top to bottom: (1) LCO i'-band light curve of the outburst of SAX J1808. (2) NICER 0.5–10 keV light curve of the outburst. (3) Absorbed $V - i'$ color trend with time during the outburst. (4) Polarization detections and upper limits in B, V, R, and I bands (VLT/FORS2). With downward arrows, the 3σ upper limits are represented with the same colors as those for the detections (dots). (5) PA vs. time. In plots (1) and (2), black arrows indicate the 3σ upper limits to the i'-band magnitude and the NICER count rate, respectively. In all plots, a dashed vertical line indicates the time of the peak of the outburst (according to X-ray observations), whereas a dotted line shows the starting time of the X-ray reflaring state. With numbers 1–9, the epochs of the polarimetric observations are indicated in all panels, as defined in Table 1.

(The data used to create this figure are available.)

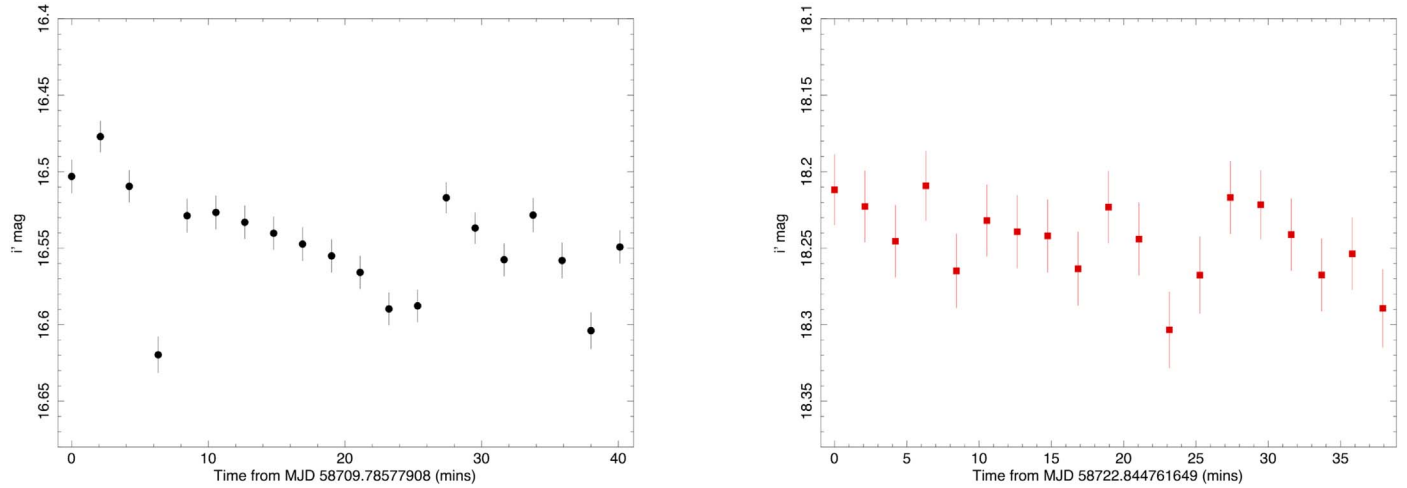

Figure 3. The i'-band light curves based on LCO data taken on MJD 58709 (2019 August 14; left panel) and 58722 (2019 August 27; right panel).

is dominated by interstellar polarization. With the interstellar polarization evaluated in the four bands, we could perform a fit of the data with the Serkowski function, which describes the interstellar polarization expected in our Galaxy (Serkowski et al. 1975):

$$\frac{P(\lambda)}{P_{\max}} = \exp^{-K\cdot\ln^2(\frac{\lambda_{\max}}{\lambda})}, \quad (5)$$

where $P_{\max}$ is the maximum value that the interstellar polarization reaches at a certain wavelength $\lambda_{\max}$, λ is expressed in micrometers, and $K = -0.10 + 1.86\lambda_{\max}$ (Wilking et al. 1982). While $P_{\max}$ is typically <5%, $\lambda_{\max}$ is normally found to be between 0.34 and 1 μm (Serkowski et al. 1975). The fit of our data with this function gave reasonable results, with $\lambda_{\max} = (0.44 \pm 0.08)$ μm and $P_{\max} = (1.18 \pm 0.08)$%. This value is compatible with the one derived in Section 3.1 (i.e., $P_{\max} <$ 1.53%) using a simplified version of the Serkowski law.

4.3. Spectral Energy Distributions

Using our LCO and VLT data, broadband spectra could be built. To obtain fluxes from the VLT polarimetric images, we first summed together the o- and e-flux measured at each angle of the HWP for the target and a group of reference stars. Then we averaged together the fluxes at the different angles. We then calibrated these fluxes using the XB-NEWS pipeline calibration performed for the LCO telescope images of the same field (see Section 3.2 for details on the XB-NEWS pipeline). The XB-NEWS i' fluxes were converted into I-band fluxes using the transformation equations in Table 3 of Jordi et al. (2006).

To de-redden the VLT and LCO fluxes, we used $A_V = 0.51 \pm 0.04$ (Di Salvo et al. 2019) and the relations of Cardelli et al. (1989) to evaluate the absorption coefficients at all wavelengths. The resulting spectra are reported in Figure 6, in comparison with the VLT polarization spectra in all epochs.

We note that the LCO and VLT observations were not taken simultaneously (see Tables 1 and 2), and therefore the spectra built starting from the two different data sets do not always agree. This is a clear sign of the presence of short-timescale variability at optical frequencies (minutes to hours; see also Figure 3).

5. The 2015 Outburst

During the 2015 outburst of SAX J1808, we obtained photometric observations in the optical (SDSS *griz*-band filters, 400–950 nm) and NIR (H band, ~1.6 μm) with the Rapid Eye Mount (REM) telescope (La Silla Observatory, Chile) on 2015 April 24 (~MJD 57136.2, i.e., during the main outburst decay; see Sanna et al. 2017 for details on the 2015 outburst evolution). A set of 12 images of 180 s integration each were acquired simultaneously in the optical bands, together with 15 images of 30 s integration each in the H band. All images were flat-field and bias corrected using standard procedures, and point-spread function photometry was performed using the `daophot` tool (Stetson 2000). Flux calibration was performed against the APASS[21] and Two Micron All Sky Survey[22] catalogs. SAX J1808 was also observed with LCO as part of the monitoring campaign performed on this source (see Section 3.2 for details). The closest observations to the REM ones were on MJD 57135.8 (April 23). We could therefore build an NIR–optical broadband spectrum of SAX J1808 (Figure 7; we note that the REM spectrum is strictly simultaneous). The spectrum shows the presence of an NIR excess, which is reminiscent of the NIR excess that was detected by Wang et al. (2001) during the 1998 outburst of the source, as shown in Figure 7 for comparison. This NIR excess hints at the emission of jets in the system, as previously noted in Wang et al. (2001). The shape of the NIR excess suggests optically thin synchrotron emission, with a possible jet spectral break in the spectrum around the J–K bands, which may extend to the radio regime (see Russell et al. 2007; Russell et al. 2008).

We also acquired polarimetric observations in the NIR (J, H bands) thanks to an accepted ESO DDT proposal (ID: 295.D-5012(A); PI: Baglio) at the NTT (La Silla Observatory, Chile) equipped with the SofI instrument. These observations were taken on 2015 April 29, 4 days after the REM observations (at the very end of the outburst decay, soon before the starting of the reflaring phase; Sanna et al. 2017). Due to the absence of a rotating HWP (see Section 3.1), the entire instrument was rotated at four different positions with respect to the telescope axis (0°, 45°, 90°, 135°) to obtain the four measurements that are necessary to evaluate the S parameter as described in

[21] https://www.aavso.org/download-apass-data
[22] http://www.ipac.caltech.edu/2mass/

Table 3
Results of the VLT/FORS2 (*BVRI* Filters) Polarimetric Campaign on the 2019 Outburst of SAX J1808

Epoch	*B*		*V*		*R*		*I*	
	P (%)	θ (°)	P (%)	θ (°)	P (%)	θ (°)	P (%)	θ (°)
1	<0.27	...	<0.31	...	...	...	...	...
2	1.49 ± 0.07	$22.13^{+1.32}_{-1.34}$	$0.78^{+0.05}_{-0.06}$	$15.71^{+2.03}_{-2}$	0.92 ± 0.05	$23.61^{+1.67}_{-1.68}$	$0.55^{+0.05}_{-0.04}$	$57.17^{+2.27}_{-2.23}$
3	$0.61^{+0.08}_{-0.07}$	$172.49^{+3.42}_{-3.36}$	$0.64^{+0.06}_{-0.05}$	26.34 ± 2.32	0.31 ± 0.05	$44.44^{+4.42}_{-4.41}$	$0.54^{+0.04}_{-0.05}$	$15.78^{+2.23}_{-2.25}$
4	$1.57^{+0.14}_{-0.13}$	$171.57^{+1.72}_{-1.9}$	2.21 ± 0.19	$12.55^{+2.20}_{-2.06}$	$1.49^{+0.12}_{-0.13}$	$30.75^{+2.80}_{-2.56}$	<0.96	...
5	0.35 ± 0.08	$5.76^{+4.82}_{-4.86}$	<0.22	...	$0.32^{+0.04}_{-0.05}$	$0.15^{+4.29}_{-4.31}$	$0.37^{+0.05}_{-0.04}$	$17.39^{+3.32}_{-3.28}$
6	<0.49	...	0.65 ± 0.07	$125.23^{+2.89}_{-3.74}$	<0.16	...	$1.60^{+0.11}_{-0.12}$	$23.12^{+1.93}_{-1.96}$
7	<0.25	...	0.44 ± 0.06	$36.95^{+3.87}_{-3.79}$	<0.17	...	0.24 ± 0.05	$28.87^{+6.09}_{-5.82}$
8	$1.03^{+0.07}_{-0.08}$	$33.32^{+2.39}_{-2.42}$	$0.4^{+0.09}_{-0.10}$	$145.53^{+6.25}_{-6.46}$	$1.03^{+0.11}_{-0.10}$	$43.73^{+2.86}_{-2.79}$	$1.10^{+0.04}_{-0.05}$	$47.47^{+1.28}_{-1.30}$
9	0.32 ± 0.07	$49.42^{+5.70}_{-5.66}$	$0.34^{+0.06}_{-0.07}$	$178.24^{+1.29}_{-4.8}$	...	...	...	...

Note. All the polarization levels and angles have been corrected for instrumental polarization. Interstellar polarization has also been subtracted, by means of a group of reference stars in the field. All the upper limits are indicated at a 3σ confidence level and have been evaluated as described in Section 3.1.

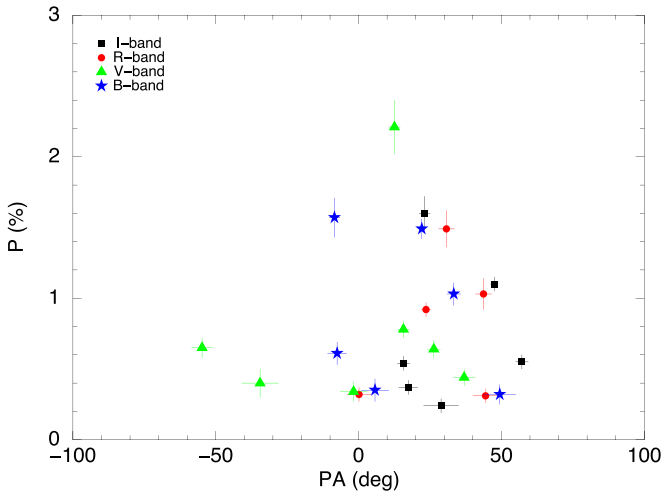

Figure 4. Polarization level P (%) vs. PA (°) in all epochs of the 2019 outburst for *I* band (black squares), *R* band (red circles), *V* band (green triangles), and *B* band (blue stars).

Section 3.1. Due to the rotation of the telescope (also the field of view was rotated for different angles), the presence of the polarimetric mask made it challenging to find a large number of reference stars that were present in every image: only five stars could be chosen as reference to correct for instrumental and interstellar effects. We note that, as SofI is mounted at the Nasmyth focus of the NTT, strong instrumental effects can be present, giving up to a few percent of polarization, depending on the direction of the observation. Images were reduced by subtracting the sky background from the frames, and aperture photometry was performed using `daophot`. Following the method described in Section 3.1, we obtained 3σ upper limits to the LP in both the *J* and *H* bands: $P_J < 1.36\%$, $P_H < 1.54\%$. Summing together the ordinary and extraordinary beams at each angle, we could obtain the flux of SAX J1808 from the SofI observations in the *J* and *H* bands. As is visible in Figure 7, the NIR excess is still evident, with fluxes slightly lower with respect to those measured in the REM observations. We therefore conclude that a jet was present during our observations, as is evident from the spectra, and the nondetection of polarization hints at very tangled magnetic fields near the base of the jet. This result is consistent with the low optical polarization measured in 2019 by VLT (see below).

6. Discussion

In this work we report on the monitoring of the recent outburst of the AMXP SAX J1808.4–3658, using different facilities and modes of observation. In particular, optical (*BVRI*) polarimetric observations have been obtained at nine different epochs during the outburst, between 2019 August 8 and 2019 September 25 (Table 1). Several detections of intrinsic LP have been made in all bands (see Table 3), all at a low level (0.2%–2.2%). The origin of the LP of the light emitted by the source must be a mechanism that is intrinsic to the source, like synchrotron from a jet and/or Thomson scattering in the disk. The interpretation of the results may vary depending on the phase of the outburst in which the target was found during the observations.

In the broadband spectrum of an LMXB, the optically thin jet spectrum is visualized as an NIR excess with respect to the low-frequency blackbody tail of the accretion disk. The jet spectrum turns over in the infrared, joining the flat or inverted spectrum at lower frequencies in the radio–millimeter band. Typically, jets in BH-LMXBs are emitted during the hard state of their outbursts and are quenched once the source transitions to the soft state. This behavior has been observed also for NS-LMXBs, such as 1RXS J180408.9–342058 (Baglio et al. 2016b; Gusinskaia et al. 2017), 4U 1728–34 (Migliari et al. 2003), and Aql X–1 (Tudose et al. 2009; Miller-Jones et al. 2010; Díaz Trigo et al. 2018), although the quenching can be less significant than that in BH-LMXBs (e.g., Migliari et al. 2004; Migliari & Fender 2006; see also Muñoz-Darias et al. 2014). SAX J1808 never leaves the hard state during its outbursts, going directly from a hard-state main outburst to a reflaring state (see, e.g., Patruno et al. 2016). The same happened during the 2019 outburst: according to our LCO monitoring, the optical outburst started on July 30; the peak of the outburst was reached on ∼August 11 (MJD 58706), and the source entered the reflaring state on August 24 (MJD 58719; Baglio et al. 2019a). Throughout this time, the X-ray spectrum was hard during both the main outburst peak and the reflaring period (Bult et al. 2019a, 2019b; Sanna et al. 2019), as is typical of faint transients. In particular, a power-law photon index of 1.89 was measured from NuSTAR observations at the outburst peak (Sanna et al. 2019), and we found that no significant variations in the hardness ratio could be observed by Swift/XRT during the whole duration of the outburst (hard

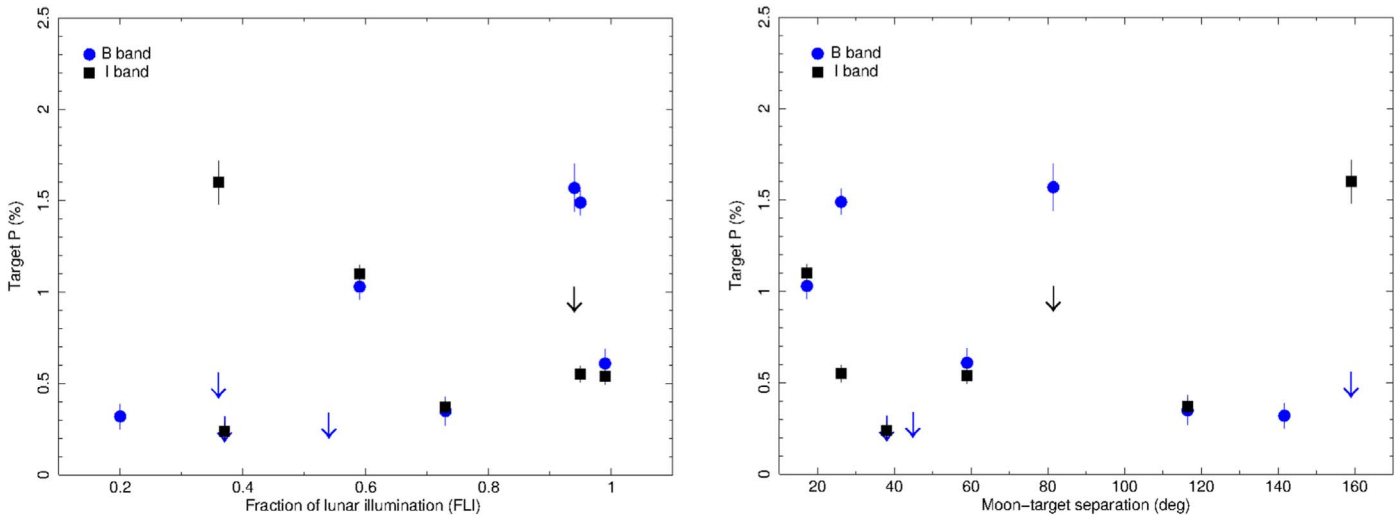

Figure 5. Left panel: *B*-band (blue dots) and *I*-band (black squares) polarization of SAX J1808 vs. FLI during the 2019 outburst. Right panel: *B*-band (blue dots) and *I*-band (black squares) polarization of SAX J1808 vs. Moon–target separation on the sky (deg). In both panels, with blue and black downward arrows we indicate the 3σ upper limits of the *B*- and *I*-band polarization levels, respectively.

band: 2–10 keV; soft band: 0.5–2 keV). Quiescence was then reached at the beginning of 2019 October (Baglio et al. 2019b).

In Figure 6 we show a comparison between the flux and polarization spectra during both the main outburst and the reflaring state. A low-frequency (z, I) excess above the blackbody tail of the accretion disk (which has a positive spectral index) is detected in several epochs (2, 3, 4, 5, 6, 8, and 9; see Figure 8 for a selection of the epochs), during both the main outburst and the flaring state, suggesting the emission of jets in the system. Epoch 1, in contrast, does not show signatures of jet emission. This is in agreement with radio observations of the target (Williams et al. 2019), according to which no jet was detected on August 4, but radio emission was observed on August 10 (i.e., between Epoch 1 and Epoch 2). Therefore, the observed optical short-timescale variability after Epoch 1 can be linked to variations in the jet (and/or in the accretion disk). Variability in the jet in particular has been observed in several LMXBs in the past, with rms up to 10%–20% in some cases (e.g., Gandhi et al. 2010, 2011; Baglio et al. 2018). This is also in agreement with the detected short-timescale variability in the i'-band light curve of MJD 58709 shown in Figure 3 (left), with a fractional rms of ∼3%. The greater prominence of this variability at the peak of the outburst than at the beginning of the flaring state (MJD 58722; Figure 3, right) suggests an origin in a jet that is variable on timescales of minutes.

We note that a certain scatter can be observed in the broadband spectra reported in Figure 6. This scatter can be explained by considering again the short-timescale variability detected in the optical band (Figure 3). From the MJD 58709 light curve, we can see that it is possible to observe a variation of ∼0.15 mag in ∼6 minutes, looking at the lowest- and highest-flux detections. Therefore, measuring a color using two filters on a similar timeframe, we could have up to a ∼0.3 mag difference, which corresponds to a factor of ∼1.3 in flux. Looking at the spectra in Figure 6, this variability can therefore explain the observed scatter. Moreover, considering that the LCO and VLT observations on the same epoch are typically separated in time by a few hours and taking into account the observed short-timescale variability, a flux change by a factor of ∼1.5 can be possible; therefore, the significant difference between the two data sets in Figure 6 can also be explained.

In Figure 9, we show the color–magnitude diagram (CMD), V versus $V - i'$, built using the LCO monitoring data. In the figure, we differentiate between the phases of the outburst (rise, decay, reflares), and we indicate the polarimetric epoch with numbers and squares in the plot. On some dates there are several $V - i'$ paired measurements; each one is shown by the epoch number (short-term variability is evident; the same polarimetric epoch has different positions in the CMD, which means that the relative disk/jet contribution changes considerably on a timescale of a few hours). With a dotted line, a blackbody model for the accretion disk is represented. This model shows the color evolution of single-temperature (as opposed to multiple temperatures from different regions), constant-area blackbody heating and cooling (for details, see Maitra & Bailyn 2008; Russell et al. 2011b; Zhang et al. 2019). At low temperatures the optical emission originates in the Rayleigh–Jeans tail of the blackbody, and at higher temperatures it originates near the curved peak of the blackbody; this causes the color changes.

We adopted the same method used by Russell et al. (2011b) to apply this model to the data of SAX J1808. The model assumes an optical extinction, $A_V = 0.51 \pm 0.04$ (see Section 3.1), to convert $V - i'$ color to an intrinsic spectral index (which is indicated on the top axis of Figure 9). The temperature depends on this color, and the normalization of the model depends on several parameters, including the size of the accretion disk (which can be estimated from the orbital period and the mass of the neutron star and companion star), the disk filling factor, the inclination angle (and potentially, disk warping), and the distance to the source. Due to uncertainties in some of these parameters and the fact that not all data of SAX J1808 are consistent with this model (see below), we did not fit the model to the data directly, but rather we varied the normalization of the model until it successfully approximated the initial brightening of the source. This part of the outburst is detailed in Goodwin et al. (2020), and it was found that the disk temperature increased from ∼7000 to ∼10,000 K during the initial optical brightening, during which hydrogen was ionized

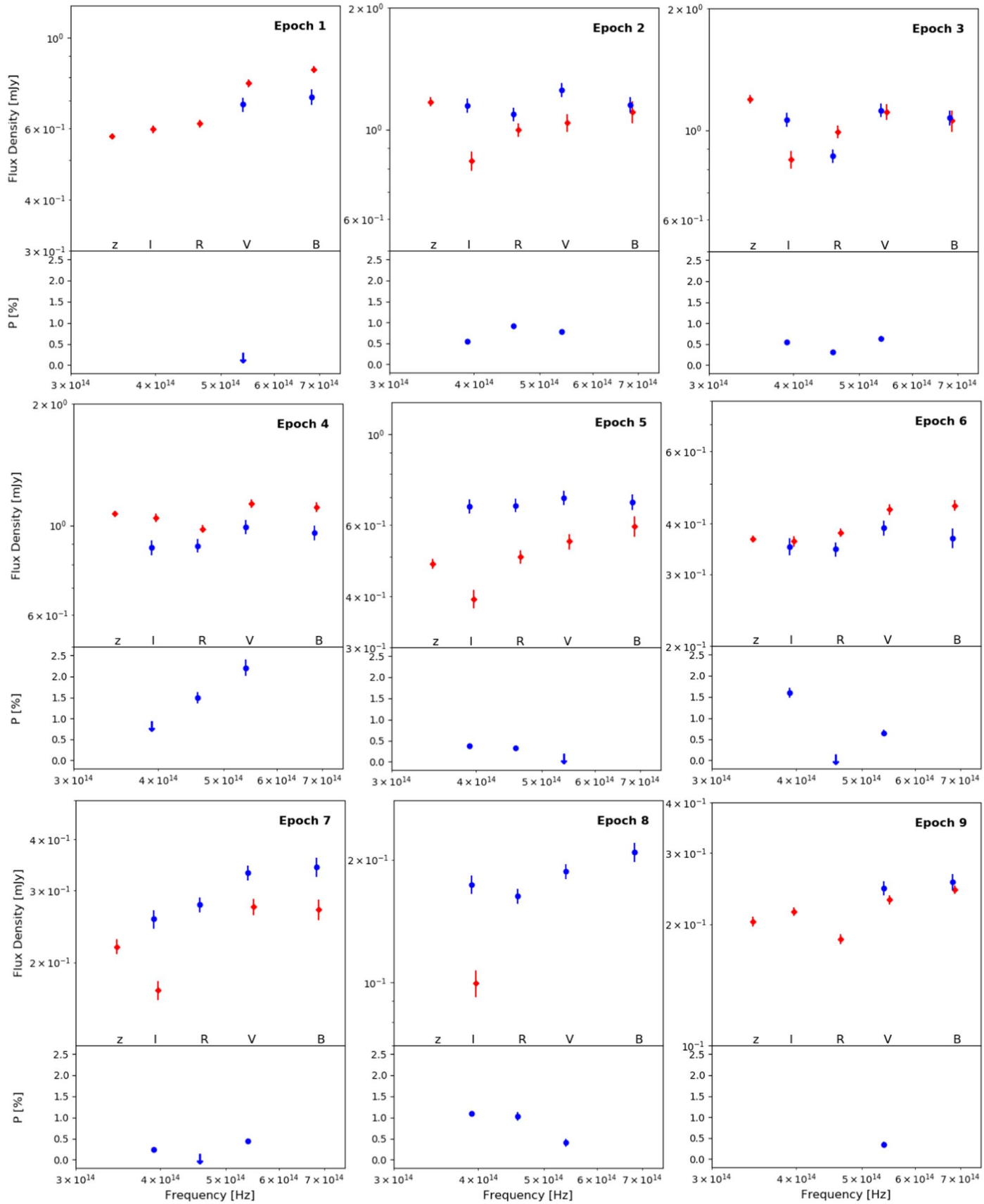

Figure 6. Upper panels: Broadband spectra of SAX J1808 obtained with Faulkes/LCO (red diamonds) and VLT/FORS2 polarimetric observations (blue circles) during the entire 2019 outburst. All fluxes have been de-reddened using $A_V = 0.51 \pm 0.04$ mag (from Di Salvo et al. 2019) and the Cardelli et al. (1989) relations. A factor of 4 in flux is represented in all plots for comparison purposes. Lower panels: Polarization spectra of SAX J1808 (blue circles). The data shown in the figures are reported in Table 3. Three-sigma upper limits to the LP are represented as blue downward arrows. *B*-band data have been excluded due to Moon contamination (see Section 4.1). We note that the polarization spectra of Epoch 4 might be affected by bad sky conditions (see Table 1).

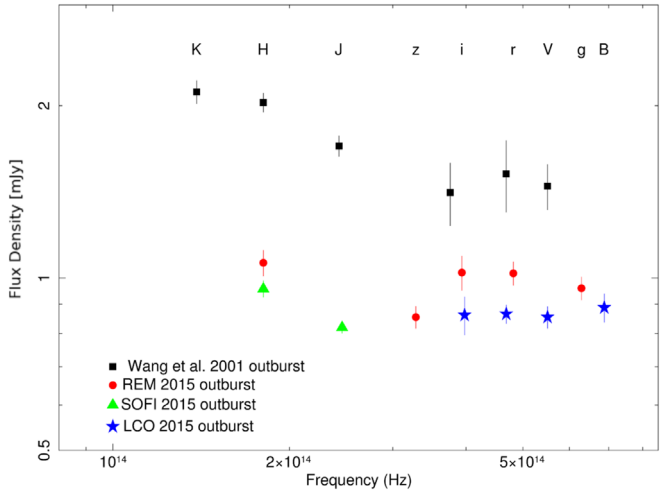

Figure 7. Broadband spectrum of SAX J1808 during previous outbursts: black squares denote the 1998 outburst reported in Wang et al. (2001); red circles, green triangles, and blue stars denote the 2015 outburst data taken with the REM telescope, the SofI instrument mounted on the NTT, and the LCO network, respectively (Section 5).

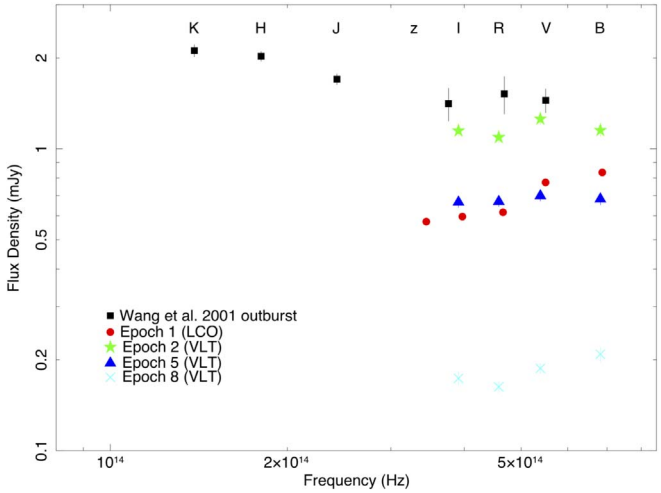

Figure 8. Broadband spectrum of SAX J1808 in four different epochs (during the 2019 outburst) for comparison: Epoch 1 during the outburst rise (LCO data), Epoch 2 during the outburst peak, Epoch 5 during the outburst decay, and Epoch 8 during the reflaring phase (VLT data). With black squares, the broadband spectrum of the 1998 outburst is reported for comparison (Wang et al. 2001). Only almost simultaneous data have been represented for clarity.

and that initiated the fast X-ray and optical rise after MJD ∼58700 (Goodwin et al. 2020).

During the first part of the rise of the main outburst, the $V - i'$ color first decreases as the disk temperature increases to >20,000 K, and then the $V - i'$ color increases, becoming redder, diverging from the blackbody model (Figure 9). After this date NIR excess is visible in the spectra (Figure 6), and the jet component appears to be responsible for the color change in the CMD. The black solid lines in Figure 9 illustrate the evolution of the data in the CMD during the outburst rise to peak. Epoch 1 is found to be close to the blackbody model, which means that the jet does not contribute considerably at that time (as is also visible in the spectrum in Figure 8, where no infrared excess and no significant LP is detected). Epochs 2–4, during the main outburst peak, have the strongest jet contribution and the strongest variability, suggesting high variability in the jet flux (and polarization; see below). Epochs 5 and 6 take place during the initial decay and have less jet contribution, but it is still considerable; Epochs 7–9 take place during the reflaring state, and a jet contribution might still be present at least in Epochs 7 and 9, but it is less significant than that during the main outburst because the data are closer to the blackbody model in the CMD (as in Epoch 1). Epoch 8 is not reported in the CMD due to the lack of LCO *V*-band data (Table 2). This behavior is reminiscent of what happened in the case of 1RXS J180408.9–342058 (Baglio et al. 2016a), where the jet did not contribute to the optical LP during the very first stages of its outburst and was instead observed a few weeks later, during the hard state of the outburst, in the broadband spectra.

Polarization detections were made during the whole outburst in different epochs and filters (except Epoch 1). As explained in Section 4.1, we excluded the *B*-band detections from the interpretation of our results, due to the contribution of the Moon, which seems to affect the results in this band. Despite the presence of low-frequency excess in the spectrum, which is consistent with the emission of optically thin synchrotron radiation (i.e., intrinsically polarized light), the detected LP in all bands is always ∼1.6% or less. This very low LP suggests that there are very tangled magnetic field lines in the emitting region, which is near the base of the jet, giving rise to strong cancellation effects and therefore to low levels of intrinsic LP. Since the magnetic field is tangled and flux variability implies a rapidly changing mass accretion rate that feeds the jet (see, e.g., Gandhi et al. 2017 and references therein), a certain variability in the LP and angle can also be expected, as we effectively observe, particularly in terms of the LP but also to some extent in terms of the PA. As shown in Figure 4, the PA clusters between ∼0° and ∼50°, except for two outlier detections in the *V* band during the reflaring state with different PAs (Epochs 6 and 8). Excluding the *B*-band observations, the PA clusters in the ∼10°–50° range, which is a small range considering the large amount of variability observed in the jet flux.

6.1. The Main Outburst Phase

In Figure 10 we show a plot of the polarization level in the *V*, *R*, and *I* bands versus the difference between the $V - i'$ observed color and the $V - i'$ color due to the disk model, shown as a dotted line in Figure 9 (the data of Epoch 4 have been removed from the figure, due to the very bad sky conditions of the night; see Table 1). The quantity reported on the *x*-axis (which we call $(V - i')_{\rm jet}$) shows how far the data are from the disk model, therefore highlighting the contribution of the jet to the total observed flux. When $(V - i')_{\rm jet} < 0.2$ mag, the polarization in all bands does not exceed 0.5%. This suggests that when the contribution from a jet is smaller, the measured LP is also lower. When $(V - i')_{\rm jet} > 0.2$ mag instead, the jet contribution is stronger, and a variable LP in the 0.3%–2% range is observed. Except for a few epochs showing higher LP (polarization flares) in the *R* and *I* bands, which interestingly all correspond to epochs in the reflaring state, a positive correlation can be found between $(V - i')_{\rm jet}$ and the LP in all three bands. Such a correlation would not be present if the disk (or any high-frequency emission component) caused the observed LP, because it would have made the polarization spectrum bluer. It seems therefore likely that the red component in the spectrum, i.e., synchrotron emission from

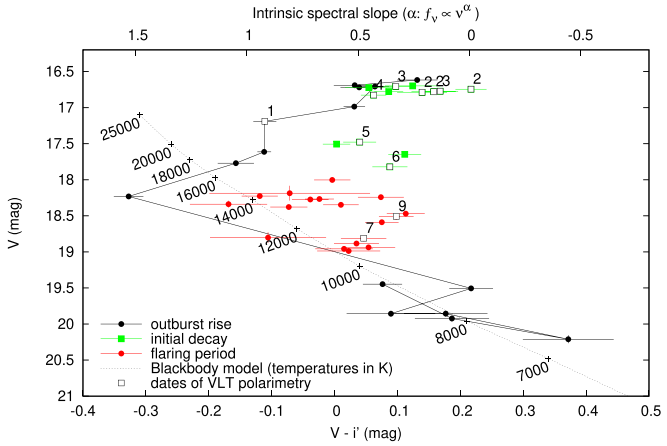

Figure 9. Optical CMD of the 2019 outburst of SAX J1808. Bluer colors (higher spectral index) are to the left, and redder colors (lower spectral index) are to the right. The three main outburst stages—the rise, initial fade, and reflaring period—are shown by black dots, green squares, and red dots, respectively. The blackbody model (see text) is shown by the black dotted line. The rise into outburst is indicated by the black solid lines joining the points. With hollow squares, the dates of VLT polarimetry are represented.

the variable jet of SAX J1808, is the cause of the LP, at least during the main outburst phase.

We notice that this correlation is true in all bands, from *I* to *V*. Therefore, this conclusion means that the jet polarization also contributes considerably in the *V* band. This may be surprising, since there is a stronger contribution from the accretion disk at those frequencies. We therefore built some simple broadband spectrum models (Figure 11) for a disk (blue line), a jet (red line), and the sum of the two components (black line), approximating the shapes of the spectra to power laws, since this is a close approximation within this small wavelength range. In particular, according to the CMD shown in Figure 9, the disk model should have a power-law index of ∼1.5 near the peak of the outburst, whereas optically thin synchrotron emission from a jet typically has a slope of ∼–0.7. Once these were fixed, we obtained three possible scenarios:

(a) The jet is brighter than the disk all the way up to the *B* band. The infrared excess is seen in the summed spectrum, getting brighter from the *V* to the *z* band. The jet contribution, as a percentage of the total flux, is shown as a number for each filter: the jet produces 84% of the flux in the *z* band, 79% in *i*′, 73% in *R*, 65% in *V*, and 53% in *B*. However this is the most extreme case, and the jet is not expected to be that bright in the optical.

(b) The jet is moderate, with the two spectra crossing over around the *R* band. The jet contribution in this case is 67% in the *z* band and 43% in the *V* band. This is a more realistic scenario, and the infrared excess is only visible as an increase in flux in the summed spectra for lower frequencies than the *z* band.

(c) The jet is faint, producing only 43% of the flux in the *z* band and 21% in the *V* band.

Scenario (b) is more realistic near the outburst peak; a summed spectrum between scenarios (a) and (b) seems to match the observed spectra in Figures 6–8. For scenario (b), if the jet is producing the polarization and the jet component is 1% polarized at all optical wavelengths (as an example), then we would expect to see 0.60% LP in the *i*′ band, 0.51% LP in the *R* band, 0.43% LP in the *V* band, and 0.31% LP in the *B* band. In particular, we notice that the *V*-band LP is ∼2/3 of the *I*-band LP, which shows quantitatively that the jet polarization should be detectable in the *V* band almost as well as in the *I* band. The relative strength of the polarized signal between different bands depends not just on the polarization of the jet and its variability but also on the spectral indices and relative flux ratios (see Figure 11) of the disk and jet.

If, on the other hand, the disk could be producing the observed LP instead of the jet, then for a disk component that is 1% polarized we would obtain 0.40% LP in the *i*′ band, 0.49% LP in the *R* band, 0.57% LP in the *V* band, and 0.69% LP in the *B* band. However, in this case we would expect the strongest LP when the data are near the disk model in the CMD (Figure 9), while the opposite is observed. We therefore interpret the observed optical polarization during the main outburst of SAX J1808 to be induced by the emission of optically thin synchrotron radiation from the compact jet in the system.

We caution the reader that the three examples shown in Figure 11 have been arbitrarily built in order to show representative cases of (a) jet-dominated, (b) moderate-jet, and (c) disk-dominated spectra. We therefore cannot draw firm conclusions from the derived numbers but can only use them as reference for our study.

6.2. The Reflaring State

The optical emission processes, and the polarization, could be different during the reflaring state. Reflares have been observed at the end of the main outburst for each of the outbursts undergone by SAX J1808 to date (Patruno et al. 2016). Such phenomena have been explained by Patruno et al. (2016) to be due to the presence of a strong outflow (caused by a propeller effect) or alternatively a trapped disk, with limited or absent outflow, in the inner regions of the disk. We know that jets are present during the reflaring state, from radio emission (Tudor et al. 2017) and the infrared excess (Figures 6, 8, and 9).

Figure 6 shows that a low-frequency excess is detected in the last two epochs (Epochs 8 and 9, following the nomenclature reported in Table 1), as well as on August 24 (Epoch 6—the first day of the reflaring state/last day of the main outburst phase), suggesting there is emission of an optically thin synchrotron from a jet also during the reflaring state. Polarization detections are also reported in this phase. The CMD in Figure 9 also shows that a contribution from the jet is still present during the flaring state (red points in the figure); however it is less prominent than during the main outburst phase. Moreover, Figure 10 (left panel) shows that a positive correlation between the measured LP in all bands and the quantity $(V - i')_{\rm jet}$ is present during both the main outburst and the reflaring state, despite the presence of three polarization flares in the *I* and *R* bands, all happening during the reflaring period. Therefore, conclusions similar to those about the main outburst phase can be drawn, with the observed LP being due to the emission of a jet in the system. The observed *I*- and *R*-band polarization flares on Epochs 6 and 8 (Figure 10, left panel) could be another manifestation of the high variability of the jet of SAX J1808, also inferred from the CMD in Figure 9. In particular, since the polarization flares are observed at low frequency only, it is likely that the component that is

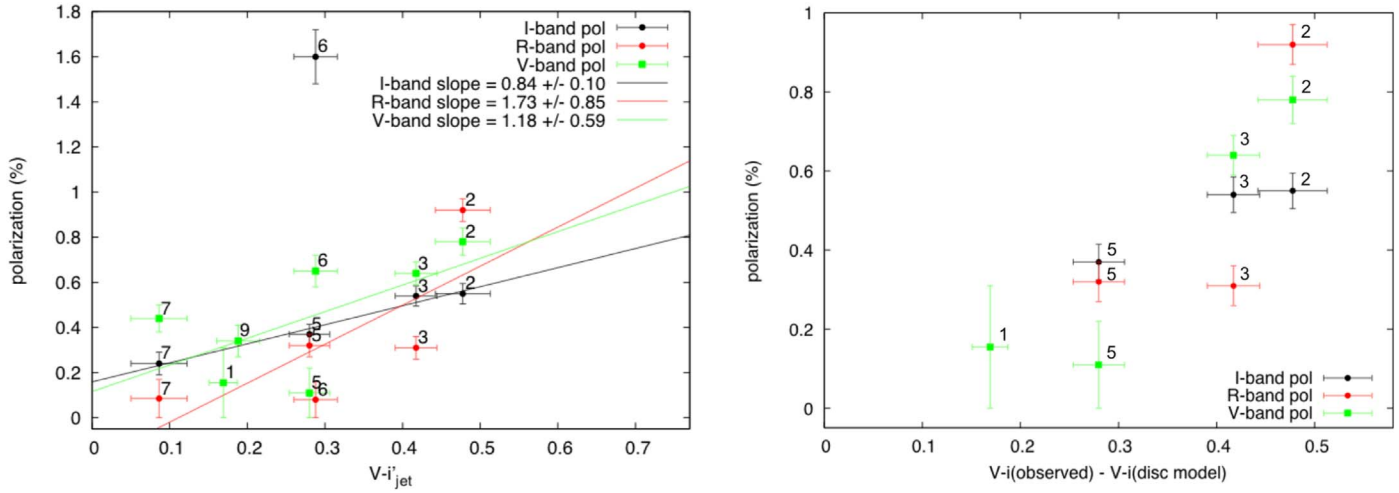

Figure 10. Left panel: Polarization level vs. $(V - i')_{\rm jet}$ for V, R, and I bands during the whole outburst. Superimposed are the linear fits to the data (the black, red, and green solid lines stand for the I, R, and V bands, respectively). The data from Epoch 4 are not reported due to the bad sky conditions of the night. Right panel: Polarization level vs. $(V - i')_{\rm jet}$ for V, R, and I bands during the main outburst (Epochs 1, 2, 3, and 5). In both panels, the epochs are clearly labeled.

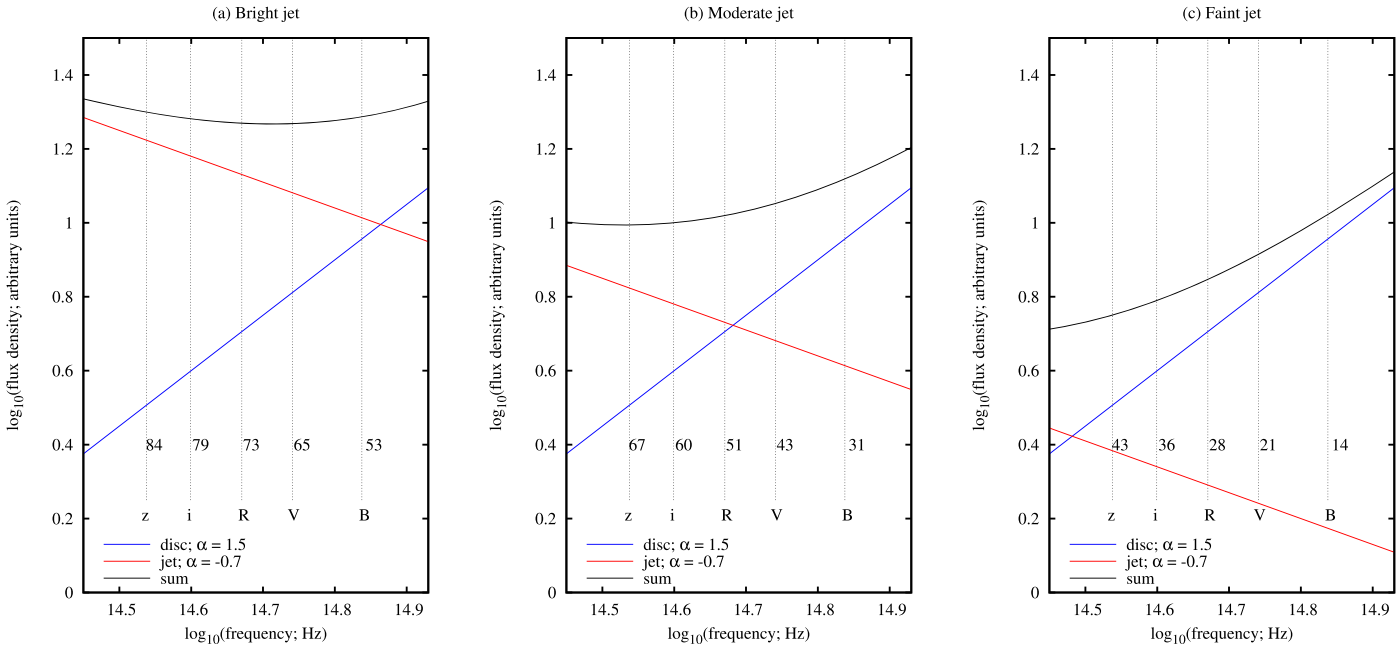

Figure 11. Broadband spectrum models for three possible configurations of jet (red line) + disk (blue line) contributions in SAX J1808 during the main outburst phase. The black solid line indicates the sum of the two components. The spectral index of the disk and jet are fixed to 1.5 and −0.7, respectively. With dotted vertical lines the central frequencies of each band are indicated. The jet contribution, as a percentage of the total flux, is indicated in each plot with numbers.

responsible for them has a red spectrum and so is due to the component that produces the infrared excess. In addition, on August 24 (Epoch 6), we only have an I-band polarization flare, with LP of 1.6%, whereas in the R band the LP on the same epoch is very low (<0.16%), and the R-band observations were performed ∼22 minutes after the I-band ones. This means that the polarization flare at this epoch was happening on a timescale of a few tens of minutes. On September 7 (Epoch 8), in contrast, the polarization flare is observed in both the I and R bands, with LP of 1%–1.1% and a lower V-band LP of ∼0.4%. This is suggestive of a red spectrum (i.e., the jet) and of a possible longer duration with respect to the flare observed in Epoch 6 (it might last longer than the full set of observations, i.e., >75 minutes).

An alternative and intriguing interpretation to the LP that is observed during the reflaring state is that it could be linked to Thomson scattering with the propelled matter. The propeller scenario is in fact used as one explanation of the reflaring activity that is observed in SAX J1808 (Patruno et al. 2016), implying the presence of matter, also in the form of free electrons, that is expelled in the form of a wide-angle outflow and can therefore scatter the light emitted by the accretion disk, giving rise to LP. The presence of propelled matter is also supported by the detection of optical and UV millisecond pulsations during the 2019 outburst, as reported in Ambrosino et al. (2020). This scenario has been invoked to explain the variable LP measured for PSR J1023+0038 by Hakala & Kajava (2018). However, if this was the case for SAX J1808,

the spectrum of its polarization flares would mimic the spectrum of the disk and be therefore bluer. Since the presence of a jet during the flaring state of SAX J1808 is proven by radio observations and by infrared excess in the spectra, we could also consider the possibility that the propelled matter might Thomson-scatter the light emitted by the jet (instead of that emitted by the accretion disk). This could give us as a result a red polarization spectrum of the reflares, similar to what we observe. However, the propelled matter typically generates a wide-angle outflow, and therefore it is unlikely that the radiation from the jet, which is collimated, can interact with it, causing Thomson scattering (and therefore LP) to happen.

In general, the observed polarization flares do not fit the main trend shown in the plot in Figure 10. Our observations are suggestive of a red spectrum also for the polarization flares (which would go against the interpretation of the observed LP being due to the Thomson scattering of disk photons in the propeller outflow), but this is hardly conclusive since we only have a few such LP flares and their spectrum on short timescales is not well constrained. If the jet is responsible for the polarization flares, then it is possible that its strong variability (supported by Figure 9 and by the variability of the spectra seen in Figure 6) is associated with a variation in the level of ordering of the magnetic field lines in the jet. A similar behavior has been observed, e.g., in the case of the NS-LMXB Sco X-1 and the BH-LMXBs GX 339–4 and V404 Cyg (Russell & Fender 2008; Russell et al. 2011a; Lipunov et al. 2016, 2019; Shahbaz et al. 2016), where strong LP variability in the NIR or optical was observed and was interpreted in terms of variability in the jet flux and/or in the conditions in the inner regions of the jet.

6.3. Magnetic Field Ordering

Since the LP is interpreted to be due to synchrotron emission from the jet, the level of ordering of the magnetic field lines f can be estimated following Bjornsson & Blumenthal (1982; see also Equation (7) of Russell & Shahbaz 2014). In particular,

$$LP(\%) = 100\, f\, \frac{1 - \alpha_{\rm thin}}{5/3 - \alpha_{\rm thin}}, \quad (6)$$

where f goes from 0 (nonuniform, tangled magnetic field lines) to 1 (uniform and aligned) and $\alpha_{\rm thin} = -0.7 \pm 0.2$ is the typical value of the optically thin synchrotron spectrum for an LMXB.

From scenario (b) of Figure 11, we see that the jet is likely contributing about ∼60% of the total flux emitted by SAX J1808 in the i' band. Considering our highest-polarization detection in the I band (1.6% in Epoch 6), this translates into an LP of the radiation emitted by the jet only in the I band of (2.7 ± 0.2)%. Using Equation (6), we therefore get $f = 0.04 \pm 0.01$. In contrast, our weakest detection (i.e., $0.24\% \pm 0.05\%$ in Epoch 7) translates into an LP of (0.4 ± 0.08)% for the jet only, from which we get $f = 0.01 \pm 0.01$. This level of ordering is lower with respect to other LMXBs (see, e.g., the LMXB GRO J1655-40, for which $f = 0.41 \pm 0.19$; Russell & Fender 2008). However, the LP measured for SAX J1808 is quite similar to the LP measured in the NIR for, for example, GX 339-4 for a jet contributing at 100% to the total emission of the source and also to the LP of the NS-LMXB Sco X-1 (Russell & Fender 2008); we therefore conclude that the low level of f measured for SAX J1808 in this work is in line with what could be inferred for other LMXBs.

A similar result can also be obtained for the 2015 outburst (Section 5). We performed a fit of the optical spectrum obtained with REM with an irradiated blackbody, and we extrapolated it to the H-band frequency, resulting in a flux density of the blackbody of 0.3 mJy in the H band. From comparison of this result with the measured flux density of SAX J1808 at the same frequency (1.1 mJy), we estimate that the jet is contributing ∼70% to the total emission of the system. Therefore, the upper limit to the LP in the H band that we report in Section 5 translates into an upper limit of 2.14% for the light emitted from the jet only. From Equation (6) we could therefore estimate the maximum level of ordering of the magnetic field, $f < 0.03$, which is very low but comparable with what we obtained for the detections of LP during the 2019 outburst.

7. Conclusions

In this work we have presented the results of a photometric and polarimetric optical campaign performed during the 2019 outburst of the AMXP SAX J1808.4–3658. The source has been found to be significantly linearly polarized in several epochs and filters, with low polarization (<2.2%, reaching down to ∼0.2% in one epoch). Moreover, a flux excess that is stronger at longer wavelengths is observed in the spectrum of the target in most epochs, which is likely due to optically thin synchrotron emission from jets. From the analysis of the $V - i'$ color compared to a blackbody disk model, we find that in general during the main outburst, when the contribution of the jet is greater (i.e., the spectrum is redder), a higher level of LP is observed. The results suggest that the observed LP during the main outburst is caused by synchrotron emission from a jet, contributing from the I band up to the V band, with variable polarization. During the reflaring phase, there is less jet contribution and, in general, less polarization, except there are some flares of polarization, with evidence suggesting they are happening on timescales of tens of minutes. The spectrum of the polarization is still red, which is suggestive of a jet origin. Other scenarios (like Thomson scattering with free electrons in the disk or in the propelled matter) can be ruled out during both the main outburst and the reflaring phase by the red spectrum of the observed polarization. We therefore conclude that the optical LP of SAX J1808 is linked to the launching of jets; in particular, the low value of polarization in all epochs and bands is a signature of strongly tangled magnetic fields near the base of the jet, with a level of ordering derived from I-band observations of 1%–4%.

Finally, the measured PA clusters around values of $\sim 30^\circ \pm 20^\circ$ during the whole campaign, implying the magnetic field vector has an angle of $\sim 120^\circ \pm 20^\circ$. In other NS- and BH-LMXBs, the magnetic field has been found in most cases to be parallel to the jet axis in this optically thin synchrotron region (Russell 2018; Shahbaz 2019 and references therein), which suggests that the jet in SAX J1808 may be launched at a position angle of $\sim 120^\circ \pm 20^\circ$. This could be tested with future high-resolution very long baseline interferometry radio observations.

In addition we have presented a short campaign performed on SAX J1808 during the 2015 outburst, with the emission of jets being detected as an NIR excess in the spectral energy

distribution during the decay of the outburst; however, no LP is observed in the NIR ($P < 1.5\%$). This can be a sign of very tangled magnetic fields at the base of the jet and/or of high variability in the jet component, as observed in the 2019 outburst. In particular, the estimated upper limit to the magnetic field ordering during the 2015 outburst is 3%, in line with what was derived for the 2019 outburst.

The polarimetric results reported here support the jet's being the origin of the NIR excess commonly observed in AMXPs and demonstrate that optical and infrared polarimetry can constrain the magnetic field structure, and its variability, close to the launching region of jets in NS-LMXBs. If such observations, including polarimetric variability studies on minute timescales, can be performed on other NS-LMXBs, this will help in uncovering the general magnetic field properties of jets in LMXBs, which can be compared to those of active galactic nuclei and other jet-launching sources.

We thank the anonymous referee for useful comments and suggestions. Based on observations collected at the ESO under ESO programs 0103.D-0575 and 295.D-5012. The Faulkes Telescope Project is an education partner of LCO. The Faulkes Telescopes are maintained and operated by LCO. We acknowledge the support of the NYU Abu Dhabi Research Enhancement Fund under grant RE124. N.M. acknowledges financial support from ASI-INAF contract No. 2017-14-H.0. T.M.D. acknowledges support via Spanish research grants RYC-2015-18148 and AYA2017-83216-P. P.D'A., S.Ca., and S.Co. acknowledge support from ASI grant I/004/11/3. P.D'A. acknowledge support from PRIN-MIUR 2017 (grant 20179ZF5KS).

ORCID iDs

M. C. Baglio https://orcid.org/0000-0003-1285-4057
D. M. Russell https://orcid.org/0000-0002-3500-631X
S. Crespi https://orcid.org/0000-0002-7441-5300
S. Covino https://orcid.org/0000-0001-9078-5507
J. Homan https://orcid.org/0000-0001-8371-2713
S. Campana https://orcid.org/0000-0001-6278-1576
F. Lewis https://orcid.org/0000-0003-3352-2334
N. Masetti https://orcid.org/0000-0001-9487-7740
A. Miraval Zanon https://orcid.org/0000-0002-0943-4484
T. Muñoz-Darias https://orcid.org/0000-0002-3348-4035

References

Alpar, M. A., Cheng, A. F., Ruderman, M. A., & Shaham, J. 1982, Natur, 300, 728
Ambrosino, F., Miraval Zanon, A., & Papitto, A. 2020, NatAs, submitted
Baglio, M. C., Campana, S., D'Avanzo, P., et al. 2015, ATel, 7469, 1
Baglio, M. C., D'Avanzo, P., Campana, S., et al. 2016a, A&A, 591, A101
Baglio, M. C., D'Avanzo, P., Campana, S., et al. 2016b, A&A, 587, A102
Baglio, M. C., D'Avanzo, P., Campana, S., & Covino, S. 2014a, A&A, 566, A9
Baglio, M. C., D'Avanzo, P., Muñoz-Darias, T., Breton, R. P., & Campana, S. 2013, A&A, 559, A42
Baglio, M. C., Mainetti, D., D'Avanzo, P., et al. 2014b, A&A, 572, A99
Baglio, M. C., Russell, D. M., Casella, P., et al. 2018, ApJ, 867, 114
Baglio, M. C., Russell, D. M., & Lewis, F. 2019a, ATel, 13103, 1
Baglio, M. C., Russell, D. M., Lewis, F., & Saikia, P. 2019b, ATel, 13162, 1
Baglio, M. C., Vincentelli, F., Campana, S., et al. 2019c, A&A, 631, A104
Bernardini, F., Russell, D. M., Shaw, A. W., et al. 2016, ApJL, 818, L5
Bildsten, L., & Chakrabarty, D. 2001, ApJ, 557, 292
Bjornsson, C. I., & Blumenthal, G. R. 1982, ApJ, 259, 805
Blandford, R., Agol, E., Broderick, A., et al. 2002, in Proc.of the XII Canary Islands Winter School of Astrophysics, Astrophysical Spectropolarimetry, ed. J. Trujillo-Bueno, F. Moreno-Insertis, & F. Sánchez (Cambridge: Cambridge Univ. Press), 177
Bramich, D. M., & Freudling, W. 2012, MNRAS, 424, 1584
Bult, P., Chakrabarty, D., Arzoumanian, Z., et al. 2020, ApJ, 898, 38
Bult, P. M., Gendreau, K. C., Arzoumanian, Z., et al. 2019a, ATel, 13077, 1
Bult, P. M., Gendreau, K. C., Arzoumanian, Z., et al. 2019b, ATel, 13001, 1
Cadolle Bel, M., Rodriguez, J., D'Avanzo, P., et al. 2011, A&A, 534, A119
Callanan, P. J., Curran, P., Filippenko, A. V., et al. 2002, ApJL, 574, L143
Campana, S., & Di Salvo, T. 2018, in The Physics and Astrophysics of Neutron Stars, Astrophysics and Space Science Library, Vol. 457, ed. L. Rezzolla et al. (Cham: Springer), 149
Cardelli, J. A., Clayton, G. C., & Mathis, J. S. 1989, ApJ, 345, 245
Chakrabarty, D., & Morgan, E. H. 1998, Natur, 394, 346
Chaty, S., Dubus, G., & Raichoor, A. 2011, A&A, 529, A3
Corbel, S., Aussel, H., Broderick, J. W., et al. 2013, MNRAS, 431, L107
Corbel, S., & Fender, R. P. 2002, ApJL, 573, L35
Covino, S., Lazzati, D., Ghisellini, G., et al. 1999, A&A, 348, L1
Deloye, C. J., Heinke, C. O., Taam, R. E., & Jonker, P. G. 2008, MNRAS, 391, 1619
Di Salvo, T., Sanna, A., Burderi, L., et al. 2019, MNRAS, 483, 767
di Serego Alighieri, S. 1997, VIIth Canary Islands Winter School of Astrophysics: Instrumentation for large telescopes (Cambridge: Cambridge Univ. Press), 287
Díaz Trigo, M., Altamirano, D., Dinçer, T., et al. 2018, A&A, 616, A23
Elebert, P., Reynolds, M. T., Callanan, P. J., et al. 2009, MNRAS, 395, 884
Falcke, H., Körding, E., & Markoff, S. 2004, A&A, 414, 895
Fender, R. P. 2001, MNRAS, 322, 31
Foight, D. R., Güver, T., Özel, F., & Slane, P. O. 2016, ApJ, 826, 66
Foreman-Mackey, D., Hogg, D. W., Lang, D., & Goodman, J. 2013, PASP, 125, 306
Gaensler, B. M., Stappers, B. W., & Getts, T. J. 1999, ApJL, 522, L117
Galloway, D. K., & Cumming, A. 2006, ApJ, 652, 559
Gandhi, P., Bachetti, M., Dhillon, V. S., et al. 2017, NatAs, 1, 859
Gandhi, P., Blain, A. W., Russell, D. M., et al. 2011, ApJL, 740, L13
Gandhi, P., Dhillon, V. S., Durant, M., et al. 2010, MNRAS, 407, 2166
Gao, F., & Han, L. 2012, Comp. Opt. and Appl., 51, 259
Giles, A. B., Greenhill, J. G., Hill, K. M., & Sand ers, E. 2005, MNRAS, 361, 1180
Gliozzi, M., Bodo, G., Ghisellini, G., Scaltriti, F., & Trussoni, E. 1998, A&A, 337, L39
Goodwin, A. J., Russell, D. M., Galloway, D. K., et al. 2019, ATel, 12993, 1
Goodwin, A. J., Russell, D. M., Galloway, D. K., et al. 2020, MNRAS, 498, 3429
Greenhill, J. G., Giles, A. B., & Coutures, C. 2006, MNRAS, 370, 1303
Gusinskaia, N. V., Deller, A. T., Hessels, J. W. T., et al. 2017, MNRAS, 470, 1871
Hakala, P., & Kajava, J. J. E. 2018, MNRAS, 474, 3297
Harrison, T. E., Gelino, D. M., Buxton, M., & Fost, T. 2014, AJ, 148, 22
Harrison, T. E., McNamara, B. J., Bornak, J., et al. 2011, ApJ, 736, 54
Hogg, D. W., & Foreman-Mackey, D. 2018, ApJS, 236, 11
Hynes, R. I., Robinson, E. L., Pearson, K. J., et al. 2006, ApJ, 651, 401
in't Zand, J. J. M., Heise, J., Muller, J. M., et al. 1998, A&A, 331, L25
Jordi, K., Grebel, E. K., & Ammon, K. 2006, A&A, 460, 339
Krauss, M. I., Wang, Z., Dullighan, A., et al. 2005, ApJ, 627, 910
Lewis, F., Russell, D. M., Fender, R. P., Roche, P., & Clark, J. S. 2008, arXiv:0811.2336
Lewis, F., Russell, D. M., Jonker, P. G., et al. 2010, A&A, 517, A72
Lipunov, V. M., Gorbovskoy, E., Kornilov, V., et al. 2016, ApJ, 833, 198
Lipunov, V. M., Kuznetsov, A. S., Gorbovskoy, E. S., et al. 2019, ARep, 63, 534
Lucy, L. B. 2016, A&A, 588, A19
Maitra, D., & Bailyn, C. D. 2008, ApJ, 688, 537
Migliari, S., & Fender, R. P. 2006, MNRAS, 366, 79
Migliari, S., Fender, R. P., Rupen, M., et al. 2003, MNRAS, 342, L67
Migliari, S., Fender, R. P., Rupen, M., et al. 2004, MNRAS, 351, 186
Migliari, S., Tomsick, J. A., Miller-Jones, J. C. A., et al. 2010, ApJ, 710, 117
Miller-Jones, J. C. A., Sivakoff, G. R., Altamirano, D., et al. 2010, ApJL, 716, L109
Muñoz-Darias, T., Fender, R. P., Motta, S. E., & Belloni, T. M. 2014, MNRAS, 443, 3270
Patruno, A., Maitra, D., Curran, P. A., et al. 2016, ApJ, 817, 100
Patruno, A., & Watts, A. L. 2012, arXiv:1206.2727

Pirbhoy, S. F., Baglio, M. C., Russell, D. M., et al. 2020, ATel, 13451, 1
Psaltis, D., & Chakrabarty, D. 1999, ApJ, 521, 332
Radhakrishnan, V., & Srinivasan, G. 1982, CSci, 51, 1096
Russell, D. 2018, Galax, 6, 3
Russell, D. M., Bramich, D. M., Lewis, F., et al. 2019a, AN, 340, 278
Russell, D. M., Casella, P., Fender, R., et al. 2011a, arXiv:1104.0837
Russell, D. M., & Fender, R. P. 2008, MNRAS, 387, 713
Russell, D. M., Fender, R. P., Jonker, P., & Maitra, D. 2008, in AIP Conf. Ser. 1068, A Decade of Accreting Millisecond X-Ray Pulsars, ed. R. Wijnands et al. (Melville, NY: AIP), 221
Russell, D. M., Fender, R. P., & Jonker, P. G. 2007, MNRAS, 379, 1108
Russell, D. M., Goodwin, A. J., Galloway, D. K., et al. 2019b, ATel, 12964, 1
Russell, T. D., Lucchini, M., Tetarenko, A. J., et al. 2020, MNRAS, submitted
Russell, D. M., Maitra, D., Dunn, R. J. H., & Fender, R. P. 2011b, MNRAS, 416, 2311
Russell, D. M., Markoff, S., Casella, P., et al. 2013a, MNRAS, 429, 815
Russell, D. M., Russell, T. D., Miller-Jones, J. C. A., et al. 2013b, ApJL, 768, L35
Russell, D. M., & Shahbaz, T. 2014, MNRAS, 438, 2083
Rybicki, G. B., & Lightman, A. P. 1979, Radiative Processes in Astrophysics (New York: Wiley)
Saikia, Payaswini, Russell, David M., Bramich, D. M., et al. 2019, ApJ, 887, 21
Sanna, A., Di Salvo, T., Burderi, L., et al. 2017, MNRAS, 471, 463
Sanna, A., Di Salvo, T., Burderi, L., et al. 2019, ATel, 13022, 1
Schultz, J., Hakala, P., & Huovelin, J. 2004, BaltA, 13, 581
Serkowski, K., Mathewson, D. S., & Ford, V. L. 1975, ApJ, 196, 261
Shahbaz, T. 2019, in Astronomical Polarisation from the Infrared to Gamma Rays, Astrophysics and Space Science Library, Vol. 460, ed. A. Słowikowska et al. (Cham: Springer), 247
Shahbaz, T., Fender, R. P., Watson, C. A., & O'Brien, K. 2008, ApJ, 672, 510
Shahbaz, T., Russell, D. M., Covino, S., et al. 2016, MNRAS, 463, 1822
Sharma, S. 2017, ARA&A, 55, 213
Srinivasan, G. 2010, NewAR, 54, 93
Stetson, P. B. 1990, PASP, 102, 932
Stetson, P. B. 2000, PASP, 112, 925
Tetarenko, A. J., Sivakoff, G. R., Miller-Jones, J. C. A., et al. 2019, MNRAS, 482, 2950
Tonry, J. L., Stubbs, C. W., Lykke, K. R., et al. 2012, ApJ, 750, 99
Torres, M. A. P., Jonker, P. G., Steeghs, D., et al. 2008, ApJ, 672, 1079
Tudor, V., Miller-Jones, J. C. A., Patruno, A., et al. 2017, MNRAS, 470, 324
Tudose, V., Fender, R. P., Linares, M., Maitra, D., & van der Klis, M. 2009, MNRAS, 400, 2111
Wang, X., & Wang, Z. 2014, ApJ, 788, 184
Wang, Z., Chakrabarty, D., Roche, P., et al. 2001, ApJL, 563, L61
Wardle, J. F. C., & Kronberg, P. P. 1974, ApJ, 194, 249
Wijnands, R., Méndez, M., Markwardt, C., et al. 2001, ApJ, 560, 892
Wijnands, R., & van der Klis, M. 1998, ATel, 17, 1
Wilking, B. A., Lebofsky, M. J., & Rieke, G. H. 1982, AJ, 87, 695
Williams, D., Motta, S., Fender, R., Woudt, P., & Miller-Jones, J. 2019, ATel, 13026, 1
Zhang, G. B., Bernardini, F., Russell, D. M., et al. 2019, ApJ, 876, 5